Chemical Engineering Journal 523 (2025) 168228

Contents lists available at ScienceDirect

Chemical Engineering Journal

journal homepage: www.elsevier.com/locate/cej

How structure-induced resonance waves intensify mass transfer in a falling film absorber for CO_2 capture

Andrea Düll [a], Andreas Happ [a], Jakob Buchmüller [a], Cihan Ateş [b], Marion Börnhorst [c], Thomas Häber [d,*], Olaf Deutschmann [a,d]

[a] Institute for Chemical Technology and Polymer Chemistry, Karlsruhe Institute of Technology (KIT), Engesserstraße 20, Karlsruhe, 76131, Germany
[b] Institute of Thermal Turbomachinery, Karlsruhe Institute of Technology (KIT), Kaiserstraße 12, Karlsruhe, 76131, Germany
[c] Institute of Reaction Engineering and Catalysis, TU Dortmund University, Emil-Figge-Straße 66, Dortmund, 44227, Germany
[d] Institute of Catalysis Research and Technology, Karlsruhe Institute of Technology (KIT), Hermann-von-Helmholtz-Platz 1, Eggenstein-Leopoldshafen, 76344, Germany

ARTICLE INFO

Keywords:
CO_2 absorption
Process intensification
Structured surfaces
Wave dynamics
VOF simulations

ABSTRACT

Efficient solvent utilization is critical in energy-intensive processes such as solvent-based carbon capture. This study adopts a combined experimental and numerical approach to investigate how surface structure modification can intensify liquid-side mass transfer in a falling film CO_2 absorber. Structure-induced resonance waves, which are found to evolve in the flow for specifically tailored structure configurations, offer significant potential in this context. The associated flow destabilization is directly reflected in the mass transfer characteristics. Compared to a smooth reference plate, a structure-induced increase in the volumetric mass transfer coefficient by up to a factor of 4.1 is achieved. Complementary numerical simulations provide new insights into the underlying mass transfer enhancement mechanisms. The wave-related increase in interfacial area plays a minor role, while changes in internal flow conditions are the dominant contributor. Most importantly, convective mixing patterns in steep wave humps transport clusters of saturated liquid from near the interface toward the less saturated bulk liquid. In contrast to solitary waves on smooth surfaces, the wave humps do not remain spatially isolated but merge back into less distorted interface regions after passing a few structure elements. This highly dynamic reconfiguration of the gas–liquid interface, along with the interplay of large- and small-scale internal mixing patterns, continuously perturbs the concentration boundary layer and promotes homogenization of the CO_2 concentration across the falling film, enabling a substantially larger fraction of the liquid phase to participate in the absorption process compared to smooth surfaces.

1. Introduction

On the path to more sustainable chemical production, process intensification plays a crucial role in reducing resource consumption, waste generation and energy demand [1]. This is of particular relevance for energy-intensive processes, such as solvent-based CO_2 capture, where the solvent regeneration requires significant amounts of thermal energy, making it the largest contributor to the process operating costs [2]. Enabling more efficient solvent use by enhancing the absorber's mass transfer characteristics is therefore expected to significantly reduce overall costs [3], which is a prerequisite for the widespread adoption of such processes at a commercial scale [4]. A similar line of reasoning applies to other energy-intensive unit operations, such as distillation [5].

Next to heat integration [5], multifunctionalization, dynamic process operation, application of centrifugal fields [6], or solvent modification [2], structure optimization for enhanced mixing and mass transfer properties is an important process intensification strategy [4,6,7]. For instance, the optimization of macroscopic and microscopic packing structures led to the development of high-performance packing internals for distillation and absorption columns, where achieving high separation efficiencies while minimizing pressure drop is crucial [7]. Similarly, the integration of vertically oriented microchannels in miniaturized falling film reactors helps stabilize the gas–liquid interface against film rupture [8], which would otherwise significantly deteriorate heat and mass transfer rates [9].

At the macro scale as well, the use of structured surfaces in falling film flow configurations receives increasing attention. Next to reactors [10], typical applications of such falling film devices include

* Corresponding author.
E-mail address: thomas.haeber@kit.edu (T. Häber).

https://doi.org/10.1016/j.cej.2025.168228
Received 19 June 2025; Received in revised form 15 August 2025; Accepted 7 September 2025
Available online 15 September 2025

evaporators [11], crystallizers [12], and absorbers [13]. Due to its thin liquid layer and large interfacial area, the falling film geometry enables high specific heat and mass transfer rates compared to other multiphase flow configurations [14]. Further advantages include short contact times, low pressure drop, and low holdup volume, which are crucial for processing heat-sensitive fluids (e.g. in the food industry), viscous liquids (e.g. in the polymer industry), and hazardous materials [15].

In the literature, findings on whether two-dimensional periodic surface structuring intensifies heat and mass transfer processes in falling film flows are not fully unambiguous. The majority of the works report enhancing effects [16–20], which are primarily attributed to a structure-induced increase in the gas–liquid interfacial area and liquid residence time [21] as well as to the formation of internal mixing zones [22]. Other studies indicate an insignificant or adverse impact [7, 23], which may result from unfavorable changes in liquid velocity and film thickness [24] when structure configurations are improperly chosen [7]. This demonstrates the need to carefully tailor the integrated surface structure configurations.

Aiming to contribute to the ongoing improvement of falling film devices, this work investigates the conditions under which such easy-to-manufacture, two-dimensional surface structures can intensify heat and mass transfer processes. In this context, the evolution of structure-induced resonance waves, studied in our previous works from a hydrodynamics perspective [25,26], holds particular innovation potential. Due to its significance in greenhouse gas reduction, the absorption of CO_2 into an aqueous liquid phase in a falling film absorber is chosen as a model system. To gain detailed insights into the enhancement mechanisms contributing to intensified mass transfer and increased absorption efficiency, experimental measurements are combined with computational fluid dynamics simulations.

2. Experimental setup and methodology

Experimental measurements are performed to gain a first overview of how the investigated surface structure configurations affect both the hydrodynamics and the mass transfer characteristics of the falling film absorber.

2.1. Falling film test rig

The employed falling film test rig is shown in Fig. 1. The working liquid is circulated by means of a micro-gear pump (LAB-ZP-12, Gather). After passing a cartridge filter (20 µm mesh size) and check valve, it is guided through an intermediate settling chamber as well as a 90 mm long and 0.6 mm thin distributor slit before entering the falling film absorber's test section. The latter has a length (x-direction), width (y-direction) and height (z-direction) of $L = 710$ mm, $W = 100$ mm and $H = 10$ mm, respectively. Counter-current gas flow of variable carbon dioxide (CO_2) and nitrogen (N_2) content is supplied by mass flow controllers (EL-FLOW Select, Bronkhorst). At the test section's downstream end, the working fluid is guided through a siphon-shaped sump (Fig. 1(b)), which maintains a stable liquid level above the outlet tube to prevent gas entrainment with the liquid. A vent is installed immediately after the sump to avoid fluctuations in fill height caused by oscillating pressure in the subsequent hose sections, which connect the falling film absorber to the liquid storage reservoirs. To allow for semi-continuous operation during physical absorption experiments, the main liquid supply loop consists of a series of three 80 L stripping tanks, which alternately serve as either uptake, regeneration or feed reservoirs. As an alternative liquid supply route for closed-loop calibration experiments, an additional 18 L gassed tank is installed. The working liquid's pH value and temperature are monitored online by pH sensors (InPro3100i, Mettler Toledo), which are installed in the absorber's inlet settling chamber and outlet sump. A pressure transducer (35X, Keller) is used to additionally monitor the gas phase pressure and temperature at the gas outlet (liquid inlet). Local time-resolved film thickness measurements can be performed using a chromatic confocal point sensor (CHRocodile 2S, Precitec) with a measurement range of 0-6 mm and maximum measurement angle of ±30° [27]. Its axial resolution is 14 nm, its linearity is 2 µm, and its lateral resolution is 7 µm [27]. For automated surface scanning, the sensor is mounted on two linear rails (Drylin SLW, Igus) with programmable motion control in the streamwise (x) and spanwise (y) directions.

2.2. Materials

Interchangeable absorber backplates with varying surface structures are machined from 12 mm thick acrylic glass sheets (Plexiglas XT, Röhm). The investigated model structure geometry is identical to that considered in our previous studies [25,26]. As shown in Fig. 1(a), it consists of arrays of rectangular ridges oriented perpendicular to the main liquid flow direction. Backplates with varying structure distance $D_s/\text{mm} \in \{2, 3, 4, 6, 8\}$ at constant structure height $H_s = 0.45$ mm as well as backplates with varying structure height $H_s/\text{mm} \in \{0.20, 0.45, 0.79, 1.20\}$ at constant structure distance $D_s = 4$ mm are investigated. Furthermore, a backplate with $D_s = 6$ mm and $H_s = 1.2$ mm, as well as a smooth reference plate, are also considered. For all surface structures, the ridge length in the streamwise direction is maintained constant at $L_s = 0.7$ mm. The specified structure parameters represent average values determined from a line scan along the entire plate length using the chromatic confocal point sensor. The corresponding manufacturing accuracy is in the order of ±15 µm.

The working liquid consists of deionized water containing sodium chloride (NaCl) at a concentration of 0.462 g/kg (8 mM). The salt was added to increase the liquid's electrical conductivity above 1000 µS/cm [28], thereby allowing for stable pH measurements. The salt's effect on other relevant thermophysical and transport properties can be considered negligible.

2.3. Experimental procedure and operating conditions

The physical absorption of CO_2 into the aqueous working liquid, hereafter simply referred to as water (H_2O) for readability, serves as the model system to evaluate the effect of varying surface structure dimensions on the mass transfer characteristics of the falling film absorber. For all backplates, absorption experiments are conducted at different gas phase CO_2 mole fractions $y_{CO_2} \in \{0.10, 0.30, 0.50, 0.75, 1.0\}$ and varying liquid phase Reynolds numbers $Re \in \{113, 228, 342, 457, 572\}$. As shown in Eq. (1), the latter is calculated from the liquid flow rate $\dot{V}$ per unit width W of the plate and the kinematic viscosity ν [29,30]. This formulation yields an average Reynolds number based on directly adjustable experimental parameters.

$$Re = \frac{q}{\nu} \quad \text{with} \quad q = \frac{\dot{V}}{W} \tag{1}$$

The gas flow rate is maintained constant at $\dot{V}_G = 5.14$ l/min and N_2 serves as the inert gas. Before the start of an experimental run, full plate wetting as well as full absorbent regeneration under a N_2 atmosphere are ensured ($pH > 5.6$). The CO_2 mole fraction in the gas phase y_{CO_2} is then gradually increased according to the discrete values listed above, and at each gas phase composition the liquid Reynolds number Re is sequentially varied. The measurement time for a single experimental setpoint is two minutes, during which pH, temperature and pressure in the absorber are continuously monitored. The outlet pH signal, which is the most sensitive to changing operating conditions and recorded at a frequency of 1 Hz, typically converges to a stable value within the first minute of measurement. Three independent absorption runs are conducted for each backplate, unless specified otherwise.

The structure effect on the falling film hydrodynamics is analyzed based on chromatic confocal point sensor measurements, which are conducted separately from the absorption runs due to differing experimental timescales. Since no systematic effect of countercurrent gas

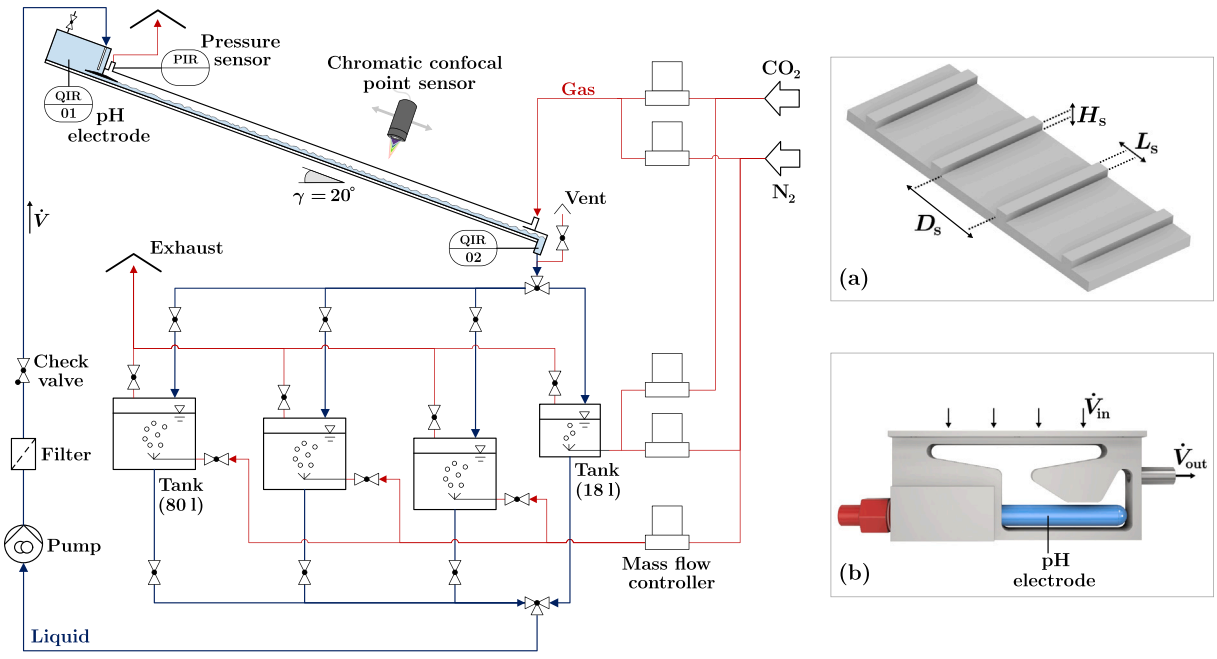

Fig. 1. Scheme of the falling film test rig with detail views of the investigated surface structure geometry (a) and the design of the absorber's liquid outlet (b). For clarity, the gas supply loop is depicted in simplified form, i.e. with a reduced number of mass flow controllers and piping complexity.

flow on the flow behavior was observed in preliminary tests for gas flow rates up to ten times higher than in the absorption experiments, the hydrodynamics investigations are carried out in the absence of gas flow and with the absorber's cover plate removed. A total of 24 measurement points are distributed across the plate's streamwise direction ($x \in \{50, 100, 200, 300, 400, 500, 600, 650\}$ mm) and spanwise direction ($y \in \{25, 50, 75\}$ mm). The temporal evolution of the gas–liquid interface is captured at each position and previously indicated Reynolds number setpoint over a duration of 20 s with a measurement frequency of 1.2 kHz.

All experiments are conducted in a climate-controlled environment at an ambient temperature and pressure around $T = 21\,°C$ and $p = 1$ bar. Only small variations in the liquid phase temperature were observed between different experimental runs ($T_{min} = 20.5\,°C$ and $T_{max} = 21.4\,°C$), and the measured temperature change in the liquid phase from inlet to outlet was below $\Delta T = 0.1\,°C$ in all experiments.

2.4. Data evaluation

The absorption of CO_2 is accompanied by a decrease in the liquid phase pH value. Assuming that the underlying reactions Appendix A are in chemical equilibrium, the pH shift can be directly related to the liquid phase CO_2 concentration. For physical CO_2 absorption, this assumption is generally valid in the case of high C-species concentrations in the liquid phase, which occur e.g. when $y_{CO2} = 1$. As increasing deviations from chemical equilibrium are expected with decreasing liquid phase C-species content, the quantitative evaluation in this study is focused on the experimental runs where the gas phase consisted of pure CO_2. The corresponding relationship $c_{CO_2} = f(pH)$ is given in Appendix B. A comparison between the equilibrium model and experimentally determined measurement points is given in Fig. 2. It underlines the good suitability of the theoretically derived data evaluation procedure under equilibrium conditions. The experimental data in the shown figure was determined in closed-loop calibration experiments, where the composition of the gas phase fed to the small 18 L tank was identical to that fed into the falling film absorber. The vent in the absorber sump was closed to avoid changes in the gas phase CO_2 content. Each discrete y_{CO_2} setpoint was maintained for a duration of 120 min to ensure convergence to a stationary state.

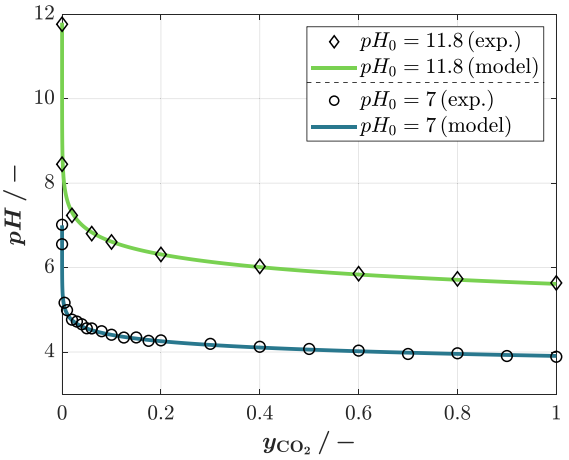

Fig. 2. pH value of the aqueous absorbent in equilibrium with a gas phase of constant CO_2 mole fraction y_{CO_2}, as determined on the basis of experimental measurements and a theoretical model for two different initial pH values pH_0. The liquid phase CO_2 saturation concentration for physically absorbed species is $c^*_{CO_2} = 0.037$ mol/l ($y_{CO_2} = 1$, $T = 21\,°C$, $p = 1$ bar).

The overall volumetric mass transfer coefficient kA is determined as a function of the liquid volume flow rate $\dot{V}$ and the liquid phase CO_2 concentration c_{CO_2} at the liquid inlet (index 'in') and liquid outlet (index 'out'):

$$kA = \dot{V} \frac{c_{CO_2,in} - c_{CO_2,out}}{\Delta c_{ln}} \tag{2}$$

The logarithmic mean concentration difference Δc_{ln} is defined in Eq. (3). The saturation concentration $c^*_{CO_2}$ is calculated from Henry's law C.1.

$$\Delta c_{ln} = \frac{(c_{CO_2} - c^*_{CO_2})_{in} - (c_{CO_2} - c^*_{CO_2})_{out}}{\ln\left(\frac{(c_{CO_2} - c^*_{CO_2})_{in}}{(c_{CO_2} - c^*_{CO_2})_{out}}\right)} \tag{3}$$

Finally, the mass transfer intensification factor ϵ_{kA} is introduced to assess the mass transfer performance of the different surface structure configurations. It is defined as the ratio between the volumetric mass transfer coefficient for a structured surface kA_{struct} and that for the smooth reference plate kA_{smooth} under identical operating conditions:

$$\epsilon_{kA} = \frac{kA_{\mathrm{struct}}}{kA_{\mathrm{smooth}}} \tag{4}$$

The evaluation of the hydrodynamic flow characteristics based on the chromatic confocal sensor measurements follows the procedure described in detail in our previous work [25]. In particular, outliers resulting from erroneous sensor measurements, which occur when the local slope of the gas–liquid interface exceeds the sensor's maximum measurement angle, are removed from the raw time series using a signal intensity threshold followed by an interquartile range filter. The standard deviation of the filtered film thickness time series is then used as the measure for film waviness, where higher standard deviations indicate intensified time-oscillatory interface motion. With regard to the uncertainty of the film thickness measurements, preliminary experiments conducted on a scaled-down hydrodynamics test rig [25] for a structured surface with a structure distance and height of D_s = 4 mm and H_s = 0.45 mm at a plate inclination angle of γ = 20.5° and a Reynolds number of Re = 332 showed that typical deviations between multiple (nine) repeated experimental runs are on the order of $\overline{h}_{\max} - \overline{h}_{\min} \approx 20\,\mu\mathrm{m}$ (2%) for the mean film thickness and $s_{h,\max} - s_{h,\min} \approx 10\,\mu\mathrm{m}$ (5%) for the film thickness standard deviation.

3. Numerical setup and methodology

To identify enhancement mechanisms contributing to the intensification of liquid-side mass transfer processes, numerical simulations are conducted using the solver *interTransportFoam* from GeoChemFoam 5.0, a toolbox based on OpenFOAM v2212 and developed for simulating reactive multiphase transport processes at the microscale [31]. It has been used in the literature, for example, to model the reactive dissolution of a CO_2 gas bubble in a pore cavity [32]. A detailed documentation of the multiphysics capabilities and numerical implementation can be found in the original works by Maes and Menke [32–34], and only a brief overview of the most relevant aspects is given here.

3.1. Problem formulation

The liquid and gas phase are considered incompressible and immiscible Newtonian fluids with constant material properties. Laminar flow is assumed and the falling film hydrodynamics, e.g. volume of the liquid and gas phase, are considered unaffected by mass transfer. The solver used in this study is derived from OpenFOAM's native *interFoam* [31]. It relies on the algebraic Volume-of-Fluid (VOF) [35] method and resolves the interface between both phases using the liquid phase volume fraction α_{L} and gas phase volume fraction $\alpha_{\mathrm{G}} = 1 - \alpha_{\mathrm{L}}$ as indicator functions [36]. The governing mass and momentum conservation equations are given below [36], where bold characters denote vector properties:

$$\nabla \cdot \mathbf{u} = 0 \tag{5}$$

$$\rho\left(\frac{\partial \mathbf{u}}{\partial t} + \mathbf{u}\cdot\nabla\mathbf{u}\right) = -\nabla p + \rho\mathbf{g} + \nabla\cdot\eta\left(\nabla\mathbf{u} + \nabla\mathbf{u}^T\right) + \mathbf{F_s} \tag{6}$$

In the equation $\mathbf{g} = -(9.22, 3.36)\,\mathrm{m^2/s}$ is the gravitational constant for a plate inclination angle of γ = 20° and $\mathbf{F_s}$ is the surface tension force. Instead of using the standard Continuous Surface Force (CSF) [37] model, $\mathbf{F_s}$ is approximated based on the Sharp Surface Force (SSF) method [36,38], which combines smoothing and sharpening of the indicator functions to reduce spurious currents [39,40]. The single-field density ρ and dynamic viscosity η are calculated from the respective gas and liquid properties as a function of the phase volume fractions with $\chi = \alpha_{\mathrm{L}}\chi_{\mathrm{L}} + \alpha_{\mathrm{G}}\chi_{\mathrm{G}}$ for $\chi \in \rho, \eta$ [36]. Furthermore, the alternative pressure term $p_{\mathrm{rgh}} = p - \rho(\mathbf{g}\cdot\mathbf{h})$ is used in OpenFoam solvers such as *interFoam* [41]. With this, the term $-\nabla p + \rho\mathbf{g}$ in Eq. (6) simplifies to $-\nabla p_{\mathrm{rgh}}$ [41].

The evolution of the gas–liquid interface is tracked by an additional advection equation (see Eq. (7)) [36]. To reduce smearing of the gas–liquid interface, the relative velocity $\mathbf{u_r} = \mathbf{u_L} - \mathbf{u_G}$ between the two phases is usually replaced by an artificial, compressive velocity $\mathbf{u_c}$ directed normal to the interface [36].

$$\frac{\partial \alpha_{\mathrm{L}}}{\partial t} + \nabla\cdot(\alpha_{\mathrm{L}}\mathbf{u}) + \nabla\cdot(\alpha_{\mathrm{L}}\alpha_{\mathrm{G}}\mathbf{u_r}) = 0 \tag{7}$$

In the *interTransportFoam* solver, multiphase species transport is implemented in single-field formulation based on the Compressive Continuous Species Transfer (CCST) method [38]. For the global concentration $c_i = \alpha_{\mathrm{L}}c_{i,\mathrm{L}} + \alpha_{\mathrm{G}}c_{i,\mathrm{G}}$ of a non-reactive species i, which represents the sum of the species concentrations in the liquid phase ($c_{i,\mathrm{L}}$) and gas phase ($c_{i,\mathrm{G}}$), the governing transport equation is given by [36,38,42]:

$$\frac{\partial c_i}{\partial t} + \mathbf{u}\cdot\nabla c_i + \nabla\cdot\mathbf{C_i} = \nabla\cdot\mathbf{J_i} \tag{8}$$

The diffusive flux $\mathbf{J_i}$ is approximated from Fick's law and an additional CST flux $\mathbf{\Phi_i}$, which results from the concentration jump at the gas–liquid interface [32,36]:

$$\mathbf{J_i} = \hat{D}_i\nabla c_i + \mathbf{\Phi_i} \tag{9}$$

In the equation, $\hat{D}_i$ is the single-field diffusion coefficient. Different formulations for $\hat{D}_i$ were proposed in the literature, including arithmetic or harmonic means of the phase-specific diffusion coefficients $D_{i,\mathrm{L}}$ and $D_{i,\mathrm{G}}$ [36,42]. The equilibrium-based mean value defined in Eq. (10) is used in the current solver version [38]. The CST flux $\mathbf{\Phi_i}$ is determined according to Eq. (11) [38], where $H_i' = c_{i,\mathrm{G}}/c_{i,\mathrm{L}}$ represents an alternative formulation of Henry constant [32]. It can be calculated from the definition in Eq. (A.2) using the ideal gas law.

$$\hat{D}_i = \frac{\alpha_{\mathrm{L}}D_{i,\mathrm{L}} + H_i'\alpha_{\mathrm{G}}D_{i,\mathrm{G}}}{\alpha_{\mathrm{L}} + H_i'\alpha_{\mathrm{G}}} \tag{10}$$

$$\Phi_i = -\hat{D}_i\frac{1 - H_i'}{\alpha_{\mathrm{L}} + H_i'\alpha_{\mathrm{G}}}c_i\nabla\alpha_{\mathrm{L}} \tag{11}$$

The expression $\mathbf{C_i}$ on the left-hand-side of Eq. (8) represents an additional compression term in the concentration equation's convective flux, which is defined in Eq. (12) [38]. It was introduced by Maes and Soulaine [36] as an extension of the standard CST method to enable more accurate simulation results with reduced numerical diffusion. This is of particular relevance for convection-dominated flows with high Peclet numbers ($Pe \geq 100$) [36], such as those considered in our study.

$$\mathbf{C_i} = \frac{(1 - H_i')c_i}{\alpha_{\mathrm{L}} + H_i'\alpha_{\mathrm{G}}}\alpha_{\mathrm{L}}\alpha_{\mathrm{G}}\mathbf{u_r} \tag{12}$$

As in standard *interFoam*, the PIMPLE (combined PISO and SIMPLE) algorithm is used for pressure–velocity coupling in the mass and momentum conservation equations (Eqs. (5)–(6)) [43]. Eq. (7), which describes the advection of the phase fraction, is solved using the Multidimensional Universal Limiter with Explicit Solution (MULES) technique to obtain a sharp interface while ensuring numerical stability and boundedness [42,44]. A sequential operator splitting approach is used to solve the species advection–diffusion equation (Eq. (8)), where advection is computed separately using MULES and subsequently introduced in the diffusion equation as a source term [38]. The time step in the simulations is dynamically adapted to satisfy a Courant number criterion of $Co < 0.25$, and is in the order of $\sim 10^{-6}$ s. The absorption simulations are carried out for several seconds of physical time ($t > 6$ s) until a quasi-steady state is achieved. An exemplary simulation case is provided in the supplementary material. Further solver-specific settings can be found there.

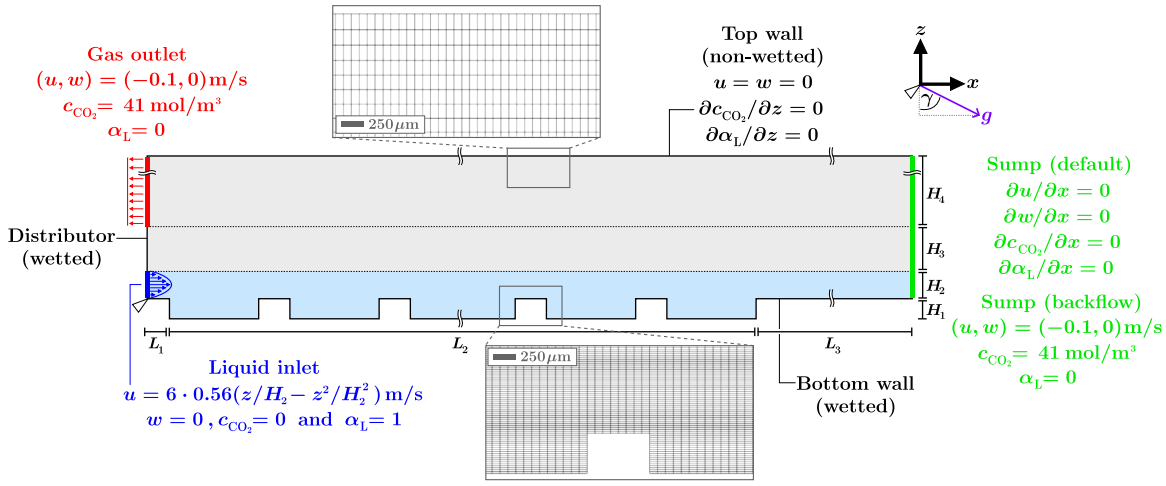

Fig. 3. Schematic representation of the numerical domain and overview of the employed boundary conditions for the velocity $\mathbf{u} = (u, w)$, the CO_2 concentration c_{CO_2} and the liquid phase fraction α_L. The origin of the coordinate system is indicated by a white triangle. $L_1 = 1$ mm, $L_2 \approx 712$ mm, $L_3 \approx 68$ mm, $H_1 = 0.45$ mm, $H_2 = 0.6$ mm, $H_3 = 1$ mm and $H_4 = 8.4$ mm.

3.2. Numerical domain

The numerical domain is shown in Fig. 3. Despite the three-dimensional nature of the evolving waves [26], only a simplified two-dimensional cross-section of the absorber is considered due to computational limitations. In the main flow direction (x), the domain consists of a smooth inlet section L_1, a structured section L_2 and a smooth outlet section L_3. The latter is elongated compared to the experimental falling film absorber to minimize the effect of the outlet boundary on the simulation results in the structured region of interest. A constant mesh size of $\lambda_x \approx 89\,\mu$m is used in the x-direction. In the z-direction, a constant mesh size of $\lambda_z \approx 23\,\mu$m is applied for domain sections H_1, H_2 and H_3, where the gas–liquid interface is expected. In domain section H_3, which is predominantly occupied by the gas phase, λ_z is gradually increased up to a maximum mesh size of 178 μm. A preliminary grid convergence study showed that the selected cell sizes provide adequate mesh resolution, with the grid convergence index for the fine-grid solution remaining below 5% for all variables of interest (Appendix D). Detail views of the numerical grid close to the wetted bottom wall and the non-wetted top wall of the absorber are shown in Fig. 3. The grid is generated automatically with ICEM CFD 2022 R2 and converted to OpenFOAM format using the *fluentMeshToFoam* utility.

3.3. Boundary conditions and material properties

The boundary conditions for the velocity $\mathbf{u} = (u, w)$, the CO_2 concentration c_{CO_2} and the liquid phase fraction α_L can be taken from Fig. 3. Since the length of the liquid distributor slit in the experimental setup significantly exceeds the hydrodynamic entrance length for developed channel flow [45], a parabolic velocity profile with a mean liquid velocity of $\bar{u} = 0.56$ m/s ($Re = 342$) is applied at the liquid inlet. As in [19], the gas velocity is, by default, specified at the gas outlet rather than at its inlet to model countercurrent gas flow. This approach is justified, firstly, because the changes in the gas phase are small and, secondly, because the gas phase behavior is of minor interest in the data evaluation. A mixed boundary conditions is used for the absorber sump, which serves as both the liquid outlet and the gas inlet. It acts as a Neumann (zero gradient) boundary condition for outward-directed flow and as a Dirichlet boundary condition for inward-directed flow, which occurs due to the suction applied at the gas outlet boundary. For such backflow, the same specifications are set as at the gas outlet. No-slip velocity boundary conditions are set at all walls. The zero-gradient boundary conditions applied to the phase fraction and species concentration at the non-wetted top wall are slightly adapted in case of the wetted distributor and bottom wall. More specifically, the derived *globalConcentrationMixed* [38] and *constantAlphaContactAngle* boundary conditions are used for c_{CO_2} and α_L, respectively. With respect to the pressure p_{rgh}, its gradient is adapted at the liquid inlet, gas outlet and wall patches in such a way that the boundary fluxes match that defined by the velocity boundary conditions. At the sump, the total pressure is set to a value of 0. Lastly, for species transport, the liquid entering the absorber is assumed to be free of absorbed CO_2. As with the velocity, the CO_2 concentration is set by default at the gas outlet, and only additionally at the sump boundary (or gas inlet) in the case of backflow into the domain. A pure gas phase with a CO_2 concentration of $c_{CO_2} = 41$ mol/m³ is considered. The latter is calculated using the ideal gas law $c_{CO_2} = y_{CO_2} p/(RT)$ with $y_{CO_2} = 1$, $p = 1$ bar and $T = 21$ °C.

As with the numerical schemes, further details on the boundary conditions can be taken from the exemplary simulation case in the supplementary material. An overview of the considered material and transport properties is given in Table 1. Regarding the gas–liquid system properties, the low salt concentration results in a negligible effect on the Henry constant, as estimated using the relations compiled in [46]. Therefore, the Henry constant H'_{CO_2} for CO_2 in pure water is used. Similarly, the surface tension of water in a CO_2 atmosphere was reported to be only about 1% lower than in an air or N_2 atmosphere at a temperature of $T = 25$ °C [47]. Consequently, literature data for the better-characterized water/air system is employed.

Table 1
Material and transport properties used in the simulation ($T = 21$ °C). The density ρ, dynamic viscosity ν and surface tension σ are taken from [48] and [49]. See Appendices C.1 and C.2 for more information on diffusivity and solubility.

Property	Unit	Liquid	Gas
ρ	kg/m³	997.99	1.81
ν	m²/s	0.9798×10^{-6}	8.1497×10^{-6}
D_{CO_2}	m²/s	1.7478×10^{-9}	1.6046×10^{-5}
H'_{CO_2}	–	1.1316	
σ	N/m	72.59×10^{-3}	

4. Experimental results and discussion

The following sections examine the effects of surface structure modification on the hydrodynamics and mass transfer characteristics

of falling film flows. In Section 4.1, experimental results on structure-induced wave evolution along the film's flow path are presented. The implications for mass transfer are then analyzed in Section 4.2 based on CO_2 absorption experiments. Complementary numerical results are provided in Section 5.

4.1. Structure-induced wave evolution

Wave evolution in falling film flows is significantly affected by the presence of surface structuring. This is visualized in Fig. 4 (a)–(c), where representative film thickness time traces $h = f(t)$ for the structured surface with a structure height of $H_s = 0.45\,\text{mm}$ and a structure distance of $D_s = 4\,\text{mm}$ are compared to those obtained for the smooth reference plate. The data was recorded at a Reynolds number of $Re = 342$ using the chromatic confocal point sensor. The measurement points are located centrally across the plate width ($y = 50\,\text{mm}$) at three different flow distances, namely close to the liquid distributor ($x = 100\,\text{mm}$), in the middle plate section ($x = 400\,\text{mm}$), and close to the liquid outlet ($x = 650\,\text{mm}$). The film thickness is given with respect to the coordinate system in Fig. 3 (z-direction), i.e. $h < 0$ indicates penetration of the gas–liquid interface into the trench between two subsequent structure elements. For the smooth reference plate, the experimentally determined mean film thickness is in good agreement with the values predicted by a literature correlation [50]. For instance, at $Re = 342$, the measured and predicted values are $\overline{h} = 712\,\mu\text{m}$ and $\overline{h} = 695\,\mu\text{m}$, respectively. This underlines the suitability of the film thickness measurement technique employed.

Regarding the emergence of transient film instabilities, significant time-oscillatory interface motion becomes visible in Fig. 4(a) for the structured surface almost immediately after the liquid enters the test section. In contrast, as can be observed in Fig. 4 (a) and (b), a prolonged entrance length exists for the smooth plate [51,52], where the gas–liquid interface remains quasi-flat. Regarding the observable wave shapes, clearly distinguishable solitary wave structures, such as the teardrop-shaped wave hump [53] in the time interval $t = 0.2\text{-}0.25\,\text{s}$ of Fig. 4(c), develop on the smooth plate after sufficient flow distance. The flow patterns evolving on the structured surface are much more chaotic, with low-frequency wave structures superimposed by high-frequency ones (Fig. 4(b)). As shown in Fig. 4(a) and (c), this complicates the identification of isolated wave fronts. Therefore, while the presence of surface structuring can amplify oscillatory interface motion, it can also weaken or even suppress long-wavelength traveling waves. In the literature, this has been linked to the occurrence of underlying steady three-dimensional wave patterns [54,55]. We observed such wave patterns in our previous work [26] for the same structure dimensions as in Fig. 4 under similar flow conditions.

As a quantitative measure for film waviness, the standard deviation s_h of the local film thickness time traces is provided in Fig. 5 as a function of the flow distance x. Results are shown for structured surfaces with a constant structure height of $H_s = 0.45\,\text{mm}$ and varying structure distance $D_s \in \{2, 3, 4, 6, 8\}\,\text{mm}$. The Reynolds number is constant at $Re = 342$. The data is averaged over the three measurement points in the spanwise (y) direction. The range between the corresponding minimum and maximum values is indicated by shading, where a significant spread would indicate partial dewetting.

The previously discussed differences between smooth and structured surfaces, such as accelerated transient flow destabilization in the presence of surface structuring and faster convergence to a developed wave state, are quantitatively reflected in Fig. 5. Irrespective of the flow distance x, the wave intensity is affected significantly by the structure distance D_s. Most importantly, an internal optimum with maximal s_h around $D_s \approx 4\,\text{mm}$ exists, at which the interface oscillations are particularly strong. As discussed in detail in our previous works [25,26], this is due to the interaction of traveling flow disturbances with an underlying statically deformed base film under resonance-like conditions. The steep increase in s_h from $x = 50\,\text{mm}$ to $x = 100\,\text{mm}$ for the structure

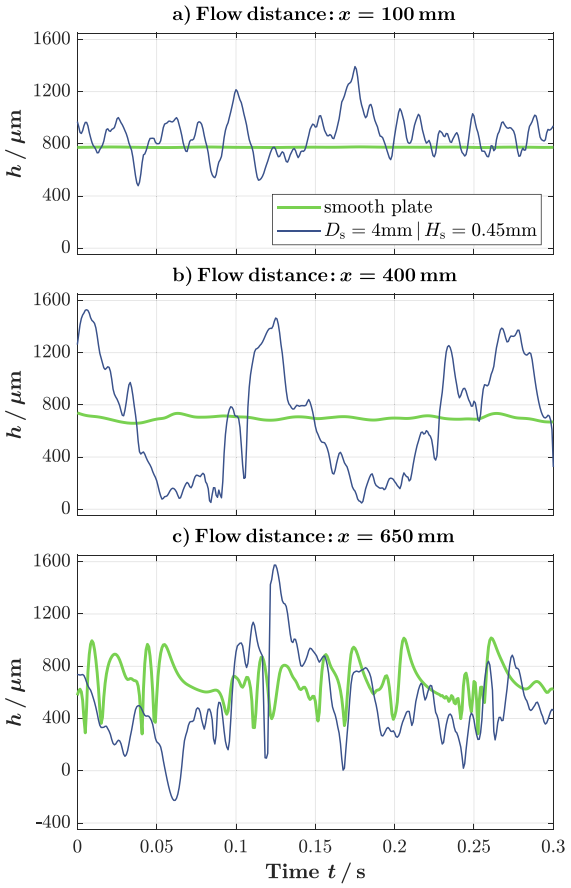

Fig. 4. Film thickness time traces $h(t)$ for falling film flow on the smooth reference plate (bright line) and the structured surface with $D_s = 4\,\text{mm}$ and $H_s = 0.45\,\text{mm}$ (dark line). The data is recorded with the chromatic confocal sensor centrally across the plate width at three different flow distance $x \in \{100, 400, 650\}\,\text{mm}$. The same abscissa applies to all subplots. $Re = 342$.

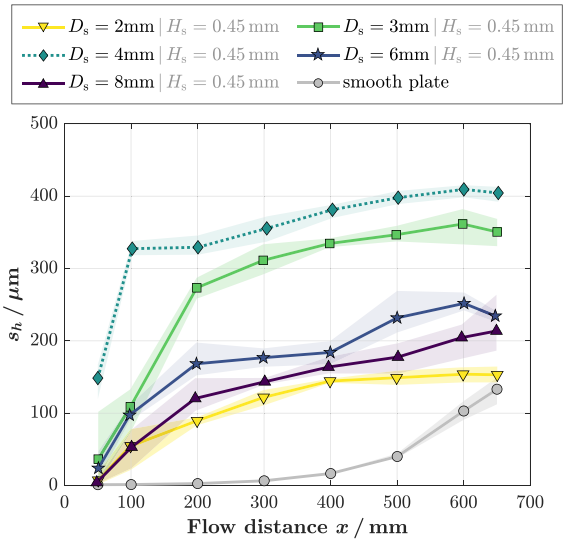

Fig. 5. Effect of structure distance on wave evolution. The film thickness standard deviation s_h is shown as a function of flow distance x for structured surfaces with constant structure height $H_s = 0.45\,\text{mm}$ and varying structure distance $D_s = 2\ldots8\,\text{mm}$, as well as for the smooth reference plate. $Re = 342$.

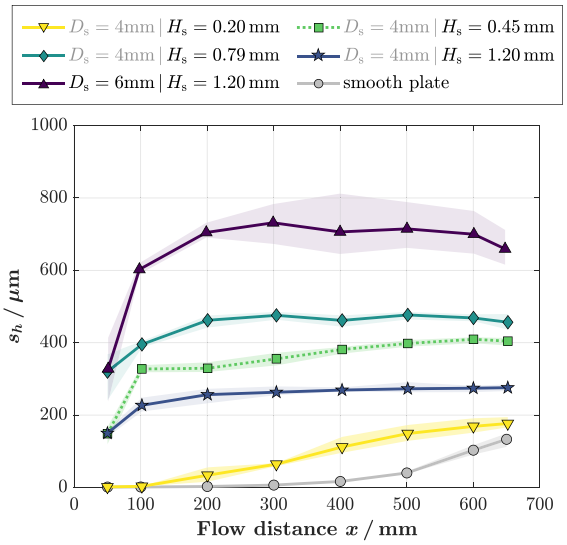

Fig. 6. Effect of structure height on wave evolution. The film thickness standard deviation s_h is shown as a function of flow distance x for structured surfaces with constant structure distance $D_s = 4\,mm$ and varying structure height $H_s = 0.2...1.2\,mm$, as well as for a structured surface with $D_s = 6\,mm$ and $H_s = 1.2\,mm$, and the smooth reference plate. $Re = 342$.

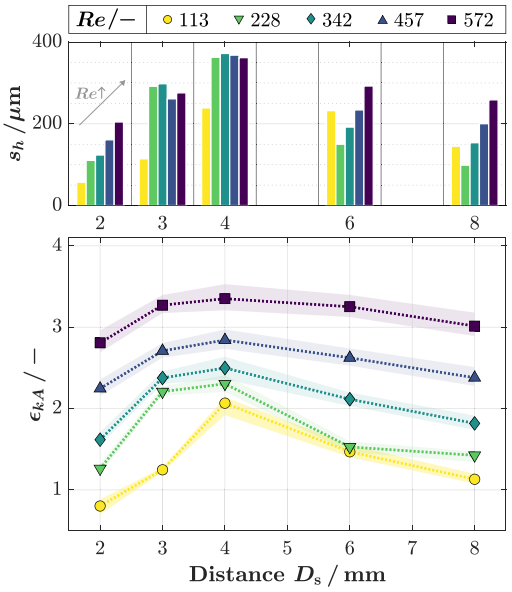

Fig. 7. Mass transfer intensification factor ϵ_{kA} (bottom) and film thickness standard deviation s_h (top) as a function of structure distance D_s at constant structure height $H_s = 0.45\,mm$. Results for five different film Reynolds numbers Re are shown. $y_{CO_2} = 1$.

distance of $D_s = 4\,mm$ additionally underlines that, under resonance conditions, transient film instabilities are not only particularly pronounced but also triggered at comparatively short flow distances. In contrast, a more gradual growth of s_h is observed for the less optimally chosen structure dimensions, and a prolonged quasi-wave-free entrance region ($s_h \to 0$) remains clearly visible for the smooth reference plate. This behavior highlights the particular potential of surface structuring for applications with limited absorber lengths.

A similar behavior can be seen in Fig. 6 for varying structure height $H_s \in \{0.2, 0.45, 0.79, 1.2\}\,mm$ at a constant structure distance of $D_s = 4\,mm$. While film waviness, as measured by the film thickness standard deviation s_h, initially intensifies with structure height up to $H_s = 0.79\,mm$, a further increase to $H_s = 1.2\,mm$ results in a sharp decline in wave intensity. Higher values of s_h under otherwise identical operating conditions can only be achieved by simultaneously increasing the structure distance D_s, as shown exemplarily in Fig. 6 for a structured surface with a structure height of $H_s = 1.2\,mm$ and structure distance of $D_s = 6\,mm$. A similar behavior was also observed in our previous work for a wider range of structure dimensions using a scaled-down hydrodynamics test rig [25]. This trend occurs because the steady wave hump induced at each individual structure element grows not only in the wall-normal (z) but also in the streamwise (x) direction as the structure height increases [56]. As a result, the surface structures must be spaced further apart for the main flow to penetrate into the trenches between adjacent ridges.

Implications of the observed flow destabilization on the mass transfer characteristics of the falling film absorber are discussed in the following section. In the analysis, the average film thickness standard deviation, calculated from the data points in Figs. 5 and 6 with $x \geq 100\,mm$, will serve as the global measure for film waviness. The measurement point closest to the liquid distributor is discarded to reduce result distortion due to entrance effects.

4.2. Mass transfer intensification

This section focuses on whether the structure-induced wave resonance effect, previously discussed with respect to the falling film hydrodynamics, is reflected in the mass transfer characteristics of the falling film absorber. Fig. 7 shows the structure-induced mass transfer intensification in comparison with the smooth reference plate as a function of structure distance D_s. In addition to the mean values calculated from three independent absorption runs (points), the experimental spread, i.e. the difference between the respective minimum and maximum values, is indicated by shading. As a measure for film waviness, the film thickness standard deviation s_h is additionally shown for every structure distance and Reynolds number in the form of a bar plot.

As shown in Fig. 7, the mass transfer characteristics of the falling film absorber are generally enhanced in the presence of surface structuring ($\epsilon_{kA} > 1$). An insignificant or even adverse impact is only seen for the lower Reynolds numbers, particularly for $Re = 113$. This can be attributed to pronounced liquid maldistribution (e.g. rivulet formation) or partial dewetting with the formation of dry patches, which occur on some of the structured surfaces below a critical liquid load. The absolute values of ϵ_{kA} are strongly affected by both the structure distance D_s and Reynolds number Re. Regarding the former, the internal optimum around $D_s \approx 4\,mm$, at which the wave intensity, or equivalently the film thickness standard deviation s_h, reaches a maximum value under resonance-like flow conditions (see Section 4.1), is directly reflected in the mass transfer intensification factor. Regarding the latter, increasing Reynolds number Re is accompanied by an increase in ϵ_{kA}. This is because the time-oscillatory interface motion remains relatively constant or is amplified with increasing Reynolds number for the structured surfaces, whereas for the smooth plate, the wave intensity decreases with increasing Re due to a longer entrance length. At the same time, the relative deviation between different structure distances diminishes at higher Reynolds numbers, which may be due to shear-induced turbulence [57] and associated mixing effects becoming more significant at higher liquid velocities. Overall, for a constant structure height of $H_s = 0.45\,mm$, the highest mass transfer intensification factor is observed at a structure distance of $D_s = 4\,mm$ and Reynolds number of $Re = 572$, where the volumetric mass transfer coefficient kA is 3.4 times higher than that determined for the smooth reference plate.

As shown in Fig. 8, the strong relationship between the wave dynamics and mass transfer characteristics is also evident for varying structure height H_s. Again, experimental results for the mass transfer

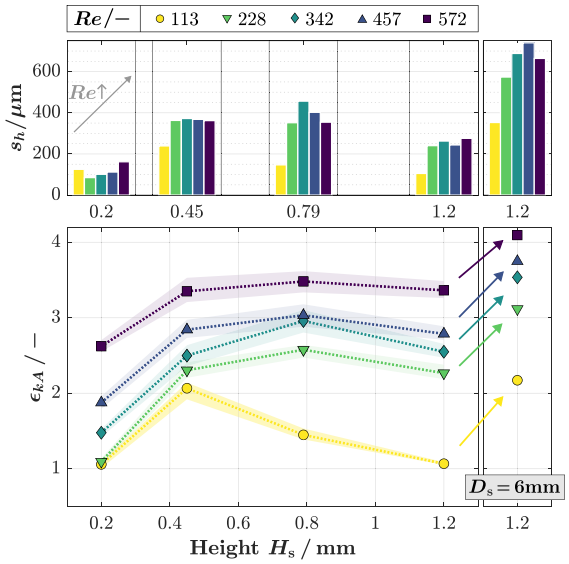

Fig. 8. Mass transfer intensification factor ϵ_{kA} (bottom) and film thickness standard deviation s_h (top) as a function of structure height H_s at constant structure distance $D_s = 4\,\text{mm}$. Additional results for a structure height of $H_s = 1.2\,\text{mm}$ and structure distance of $D_s = 6\,\text{mm}$ are shown on the right hand side of the plot. The data is given for five different film Reynolds numbers Re. $y_{CO_2} = 1$.

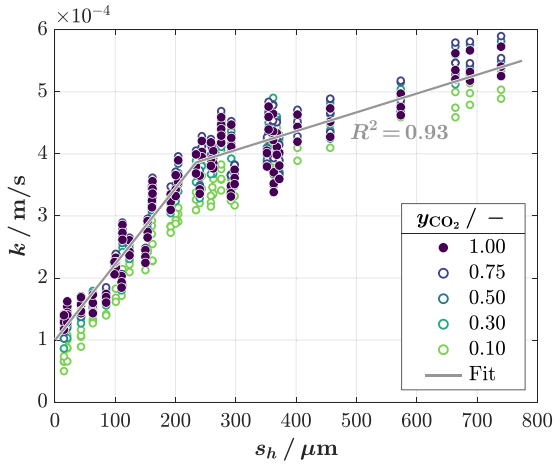

Fig. 9. Mass transfer coefficient k as a function of the film thickness standard deviation s_h. k is estimated from the volumetric mass transfer coefficient kA assuming $A = 0.071\,\text{m}^2$. Results for varying structure height H_s, structure distance D_s, Reynolds number $Re > 113$ and gas phase composition y_{CO_2} are shown.

intensification factor ϵ_{kA} (scatter plot) and film thickness standard deviation s_h (bar plot) are shown. Most importantly, as discussed with respect to the wave intensity in Section 4.1, an increase in H_s must be accompanied by an increase in the structure distance D_s to further intensify liquid-side mass transfer. For instance, at a Reynolds number of $Re = 572$, the mass transfer intensification factor remains roughly constant at $\epsilon_{kA} \approx 3.4$ when the structure height is increased from $H_s = 0.45\,\text{mm}$ to $H_s = 1.2\,\text{mm}$ at constant structure distance. However, extending the structure distance from $D_s = 4\,\text{mm}$ to $D_s = 6\,\text{mm}$ at $H_s = 1.2\,\text{mm}$ results in an increase in ϵ_{kA} by 21% up to a value of $\epsilon_{kA} \approx 4.1$. While a corresponding optimal structure distance-to-height ratio D_s/H_s exists, it is itself dependent on the structure height [25].

The results from all absorption experiments conducted in this study are compiled in Fig. 9, where the mass transfer coefficient k is plotted as a function of the film thickness standard deviation s_h. To estimate k from the volumetric mass transfer coefficient kA, an ideally smooth liquid film with an interfacial area of $A = 0.071\,\text{m}^2$ is assumed. The mass transfer coefficients thereby determined for the smooth reference plate are of the same order of magnitude as those commonly reported in the literature [58]. For instance, at $Re = 342$, an experimental value of $k = 1.5 \times 10^{-4}\,\text{m/s}$ is obtained, while the mass transfer correlation reported in [30] yields a predicted value of $k = 9 \times 10^{-5}\,\text{m/s}$. Deviations in absolute values may arise from differences in the geometry of the employed absorber (tubular versus planar), as well as from sidewall or entrance effects [7,30]. Next to the smooth reference values, Fig. 9 contains experimental results for varying structure height H_s, structure distance D_s and Reynolds number Re, with only data obtained for $Re = 113$ discarded due to the occurrence of significant liquid maldistribution. In addition to the previously analyzed results for a pure CO_2 gas phase ($y_{CO_2} = 1$, filled circles), supplementary data for CO_2/N_2 mixtures ($y_{CO_2} < 1$, open circles) is also shown. The results for the different gas phase compositions are in good agreement, indicating that the previously discussed structure-induced mass transfer intensification also applies to conditions, where the gas phase partial pressure of the species to be absorbed is reduced.

As can be seen in Fig. 9, the mass transfer coefficient k is directly proportional to the film thickness standard deviation s_h. The corresponding piecewise fit function, determined from the data points in Fig. 9 with $y_{CO_2} = 1$, is given in Eq. (13). As indicated by the two different slopes, the potential for wave-induced mass transfer intensification is greatest at low initial film waviness (or s_h) and slightly reduced at higher s_h. The associated mass transfer enhancement mechanisms are discussed in the following section based on a numerical simulation study.

$$k \times 10^6\,\frac{\text{m}}{\text{s}} = \begin{cases} 1.23\,\dfrac{s_h}{\mu\text{m}} + 99.56 & , s_h \le 234\ \mu\text{m} \\ 0.30\,\dfrac{s_h}{\mu\text{m}} + 315.40 & , s_h > 234\ \mu\text{m} \end{cases} \tag{13}$$

5. Numerical results and discussion

The numerical simulation setup described in Section 3 is used to investigate the enhancement mechanisms contributing to the experimentally observed structure-induced mass transfer intensification. After a comparison between experimental and numerical results in Section 5.1, the enhancement mechanisms are discussed in Section 5.2. Finally, in Section 5.3, the effect of surface structuring on the liquid residence time distribution of the absorber is analyzed.

5.1. Comparison with experiments

For an initial validation of the simplified two-dimensional model, the numerical results are compared against experimental measurements. Fig. 10 presents this comparison for the two key output parameters, namely the mass transfer intensification factor ϵ_{kA} (a) and the film thickness standard deviation s_h (b). The data are given as a function of structure distance D_s for a constant structure height of $H_s = 0.45\,\text{mm}$ and Reynolds number of $Re = 342$.

The structure-induced mass transfer enhancement, as quantified by ϵ_{kA} in Fig. 10(a), is slightly underpredicted compared to the experimental results. This may be attributed to neglected three-dimensional effects, such as convective mixing structures in the spanwise direction. Conversely, the transient interface motion, as quantified by the film thickness standard deviation s_h in Fig. 10(b), is usually overpredicted. This may also be due to the simplified two-dimensional numerical domain, as the evolution of three-dimensional wave patterns from steep two-dimensional wave fronts can be accompanied by a reduction in the overall wave height [55]. Additionally, in terms of the statistical data evaluation, the reduced sample size of the numerical results ($\sim 10^2$ data points) compared to the experimental results ($\sim 10^3$ statistically

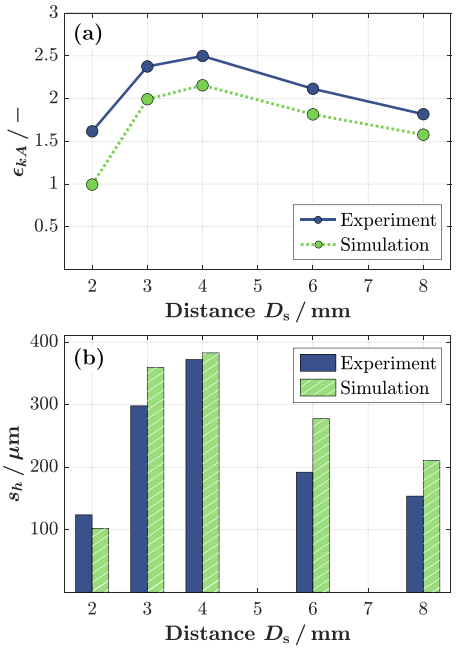

Fig. 10. Comparison between experimental measurements and numerical simulations with respect to the mass transfer intensification factor ϵ_{kA} (a) and the film thickness standard deviation s_h (b). $H_s = 0.45$ mm and $Re = 342$.

independent data points) could also contribute to the differences in s_h. Despite these local differences, the general trends observed in the absorption experiments are well reflected in the numerical simulations. Most importantly, the simulations capture the existence of an optimal structure distance around $D_s = 4$ mm, where both the intensity of the structure-induced interface oscillations and the mass transfer enhancement are most pronounced, as quantified by internal peaks in s_h and ϵ_{kA}. Consequently, although the spatial domain has been significantly simplified, the numerical simulation setup is considered suitable for analyzing the underlying enhancement mechanisms contributing to the structure-induced mass transfer intensification, as observed both experimentally and numerically.

5.2. Mass transfer enhancement mechanisms

The gas–liquid interfacial area A directly contributes to the volumetric mass transfer coefficient kA. Its structure-induced increase relative to the smooth reference plate is shown in Fig. 11 as a function of structure distance D_s. Since the results are derived from two-dimensional simulations, the additional area increase due to interface modulations in the third dimension is neglected. Compared to the mass transfer intensification factor ϵ_{kA} in Fig. 10(a), a similar trend with an internal maximum at a structure distance of $D_s = 4$ mm can be observed for ϵ_A, as the ratio between the gas–liquid interfacial area on the structured surfaces and the smooth plate. However, while the factors by which surface structuring increases the interface are typically in the range of $\sim 10^{-2}$, the corresponding values for the volumetric mass transfer coefficient are significantly higher and in the order of $\sim 10^{0}$. Therefore, provided that the falling film wall is fully wetted at all times, it can be concluded that the structure-induced increase in interfacial area plays a minor role in the overall mass transfer enhancement. Consequently, changes in the internal flow conditions are a much more dominant contributor, and they are analyzed in detail in the following.

Fig. 12 compares the wave dynamics observed for the structured surface with $D_s = 4$ mm and $H_s = 0.45$ mm (right column) to those seen for the smooth reference plate (left column). The subplots show the spatial distribution of the CO_2 concentration within the liquid film

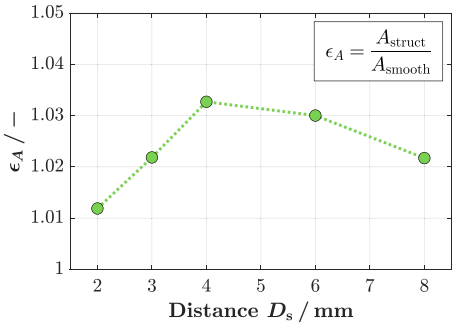

Fig. 11. Structure-induced increase in the gas–liquid interfacial area with respect to film flow on the smooth reference plate. $H_s = 0.45$ mm and $Re = 342$.

at flow distances around $x = 190$ mm for the former and around $x = 580$ mm for the latter, as significant interfacial waves develop on the smooth surface only much further downstream. The data is given in dimensionless form relative to the CO_2 saturation concentration $c^*_{CO_2}$. The time interval between the two series of snapshots (a)–(c) and (d)–(f) is 0.01 s.

As shown in Fig. 12(a)–(c), the wavy film flow on the smooth reference plate consists of large wave humps, which travel on an underlying quasi-smooth bulk film. Large moving-frame vortices in each of the solitary wave humps contribute to enhanced gas absorption in comparison to non-wavy flow conditions [59]. These vortex structures are too weak to be observed in the wall-fixed reference frame, but they can be visualized by streamlines in a reference frame translated at wave speed [53]. An example is shown in Fig. 12(c). The location where the reference velocity is extracted is marked with an arrow. The vortex visibly disturbs the concentration distribution near the gas–liquid interface, both at the front and at the back of the wave hump. However, the underlying bulk film remains largely unaffected by these convective mixing patterns, and liquid motion perpendicular to the main flow direction is barely observed. Therefore, despite the wavy interface motion, liquid redistribution is limited to only a portion of the liquid phase and homogenization of the CO_2 concentration across the entire film is not expected in the case of the smooth reference plate. Moreover, as described by Dietze et al. [59], the wave-induced mass transfer enhancement will deteriorate once the liquid in the main wave humps is fully saturated with CO_2.

As already observed experimentally (Section 4.1), the wave dynamics observed on structured surfaces are significantly different to those on the smooth reference plate. As shown in Fig. 12(d)–(f), the presence of surface structuring induces highly transient interface motion even at small flow distances. Particularly steep wave fronts typically develop upstream of localized flow reversal zones. The latter can occur in the presence of high interface curvatures, where streamwise pressure gradients become significant [60]. Examples of flow reversal zones are marked in the three subplots by arrows. In the wall-fixed reference frame, they appear as cellular streamline patterns between the interface and the solid wall. At the front of the large wave humps, streaks of CO_2-rich liquid are extracted from near the interface and convectively transported toward the solid wall, where the liquid is considerably less saturated. In turn, CO_2-lean liquid is transported from the regions within the trenches toward the gas–liquid interface at the back of the wave hump. This leads to an effective disturbance of the concentration boundary layer. A similar phenomenon was observed in the literature for periodically forced film flows on a corrugated wall [59]. The occurrence of such large-scale convective mixing patterns is associated with pronounced pressure gradients within the liquid film. This is illustrated in Fig. 13, where the pronounced local pressure minimum linked to the flow reversal zone [61] is clearly visible. Additionally, smaller recirculation zones are present within the flow. As visualized

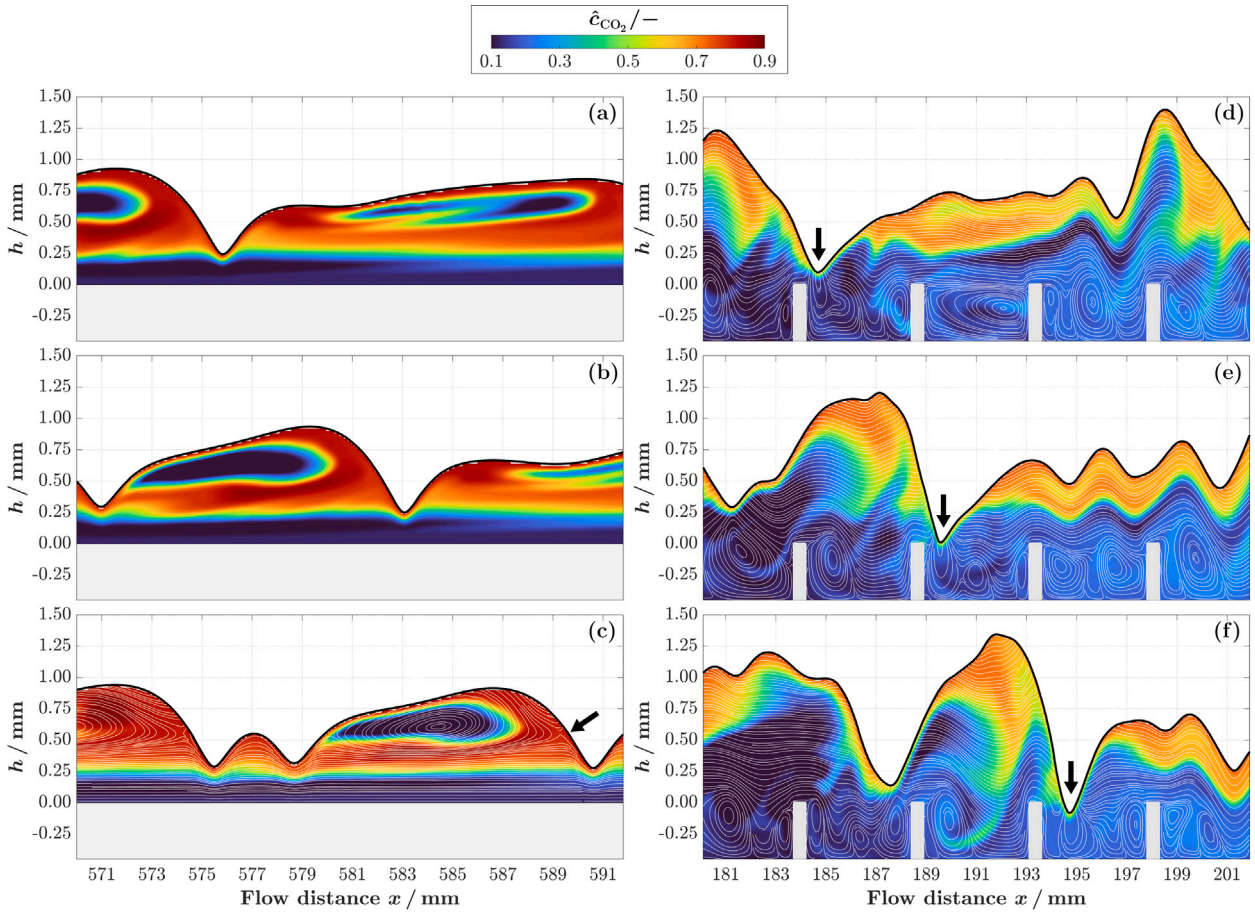

Fig. 12. Spatial distribution of the dimensionless CO_2 concentration $\hat{c}_{CO_2} = c_{CO_2}/c^*_{CO_2}$ for the smooth reference plate (left) and the structured surface with $D_s = 4\,mm$ and $H_s = 0.45\,mm$ (right). Subplots (a)–(c) and (d)–(e) show consecutive time steps with a time difference of 0.01 s. The streamlines in (c) are visualized in a wave-fixed reference frame and those in (d)–(e) in a wall-fixed reference frame. $Re = 342$.

by the streamlines in Fig. 12 (d)–(f), they occur primarily in the vicinity of the structure elements and contribute to local liquid mixing within the trenches.

In contrast to solitary waves on smooth surfaces, which eventually propagate in a wave-fixed stationary state, the large wave humps that develop on structured surfaces do not remain spatially isolated. Instead, they merge back into less distorted wave structures after passing a few structure elements. This highly dynamic reconfiguration of the gas–liquid interface, as well as the interplay between large-scale and small-scale internal mixing structures, leads to a continuous disruption of the concentration boundary layer and a gradual reduction of the CO_2 concentration differences across the liquid film. This ensures an efficient utilization of the liquid phase in the absorption process. The effect is particularly pronounced when the structure dimensions are chosen such that strongly oscillating interface motion is induced under resonance-like conditions.

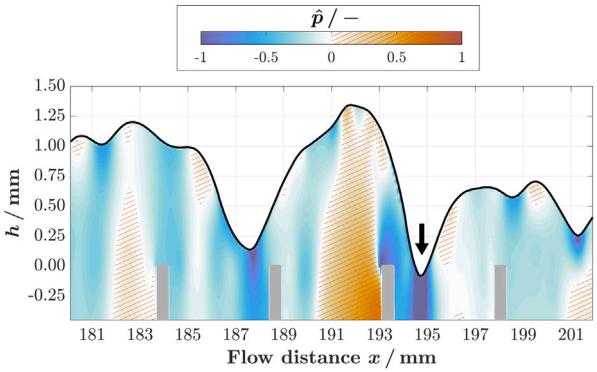

Fig. 13. Pressure distribution for case (c) in Fig. 12. The data is given in dimensionless form relative to $p_{ref} = 100\,Pa$.

5.3. Structure effect on residence time behavior

The structure-induced mixing effects described in Section 5.2 significantly affect the liquid residence time behavior in the falling film absorber. This is discussed below based on a series of additional numerical simulations of non-diffusive tracer transport. The simulations are performed at a Reynolds number of $Re = 342$ for the smooth reference plate as well as for the structured surface with $D_s = 4\,mm$ and $H_s = 0.45\,mm$, where particularly pronounced mass transfer enhancement was observed in the CO_2 absorption experiments. The same numerical setup as described in Section 3 is used, but the diffusion coefficients D_{CO_2} in both phases and the Henry constant H'_{CO_2} are set to negligibly small values to eliminate diffusion effects and restrict tracer transport to the liquid phase. The simulations are initialized from a hydrodynamically developed state with a completely tracer-free liquid phase. The tracer species is injected at the liquid inlet at a constant concentration ($c_{T,in}$) over a time interval of $t = 0.15\,s$. The start time ($t = 0$) is defined as the time when 50% of the total amount of tracer ($N_{T,in}$) has been injected into the domain. The residence time τ is defined in a similar manner and determined as the time at which 50% of the total injected tracer has passed a given probe location.

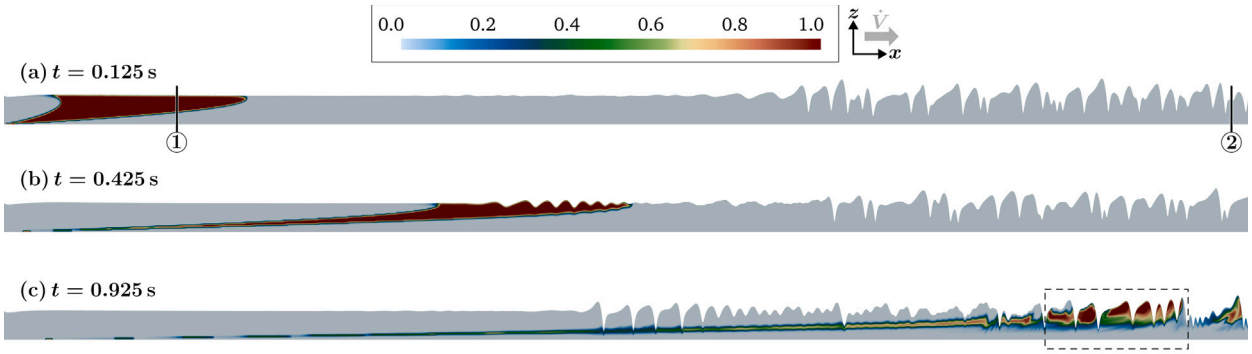

Fig. 14. Spatial distribution of the non-dimensional tracer concentration $\hat{c}_T = c_T/c_{T,in}$ for falling film flow on the smooth reference plate at $Re = 342$. Results are shown in subfigures (a)–(c) for three different time steps t. The domain is stretched by a factor of 25 in the z-direction.

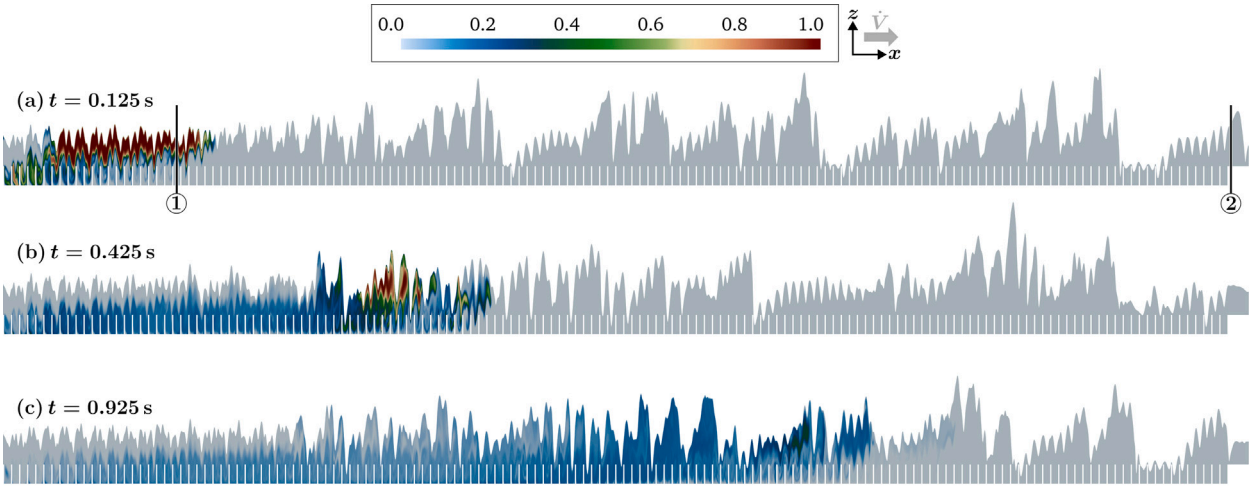

Fig. 15. Spatial distribution of the non-dimensional tracer concentration $\hat{c}_T = c_T/c_{T,in}$ for falling film flow on the structured surface with $D_s = 4\,\text{mm}$ and $H_s = 0.45\,\text{mm}$ at $Re = 342$. Results are shown in subfigures (a)–(c) for three different time steps t. The domain is stretched by a factor of 25 in the z-direction.

Figs. 14 and 15 provide an overview of the spatio-temporal evolution of the tracer concentration for falling film flow on the smooth and structured surfaces, respectively. The results are given in dimensionless form relative to the inlet tracer concentration and a non-linear color map is used to make even low tracer concentrations easily visible. The individual subplots (a)–(c) represent three different time instances.

As shown in Fig. 14(a), the gas–liquid interface near the liquid inlet remains quasi-flat in the absence of surface structuring, and the tracer pulse retains a compact shape. This is quantified in Fig. 16(a), where the instantaneous tracer concentration averaged over the film thickness (left axis) and the cumulative amount of tracer passed (right axis) are plotted as a function of time. The data is non-dimensionalized with respect to the inlet tracer concentration or total amount of injected species. It is sampled at the probe line 1, which is located at a flow distance of $x \approx 100\,\text{mm}$ from the liquid inlet. The presence of surface structuring immediately alters the shape of the tracer pulse. From Fig. 15(a), it can be observed that immediately after the liquid inlet, streaks of high tracer concentrations are convectively transported into the trenches between neighboring structure elements, where they mix with tracer-lean liquid. The corresponding mechanisms were described in detail in Section 5.2 in the context of CO_2 absorption. From a quantitative perspective, as presented in Fig. 16(b) for probe line 1, this is reflected in slight oscillations in the main tracer pulse and the development of an elongated tail section at $t > 0.27\,\text{s}$.

The same structure-induced mixing effects persist along the entire flow path. Fig. 15 (b) and (c) demonstrate that this results in a significant homogenization of the tracer concentration across the liquid film at later time steps. In contrast, as shown in Fig. 14 (b) and (c), the tracer pulse remains considerably more isolated from the surrounding liquid in the case of the smooth reference plate. This also applies as interfacial waves form at larger flow distances, where the tracer species is effectively transported in the form of individual clusters within elevated wave humps. This is evident, for example, in the flow section marked by the dashed rectangle in Fig. 14(c). Thus, the separation between the flow within the large interfacial wave structures and the underlying bulk film described in Section 5.2 is clearly reflected in the residence time behavior. The visually observed discrepancies between the flow dynamics on the smooth and the structured surface are quantified in Fig. 17. The representation is similar to that in Fig. 16, but the data is sampled at probe line 2 in Fig. 14(a), which is located near the liquid outlet ($x = 716\,\text{mm}$). In the case of the smooth surface in subplot (a), the tracer pulse (left axis) becomes highly irregular, exhibiting strong temporal oscillations in the sampled tracer concentration due to the traveling wave humps containing spatially separated clusters of highly concentrated tracer. The overall tracer residence time determined at probe line 2 for the smooth surface ($\tau = 1.1\,\text{s}$) is slightly lower, but still within the same value range as the one theoretically calculated from the mean film velocity ($\tau = 1.3\,\text{s}$). In contrast, in the case of the structured surface in subplot (b), the original pulse shape is barely visible. The structure-induced homogenization of the concentration field across the liquid film, combined with the penetration of tracer into regions of considerably decelerated flow, such as the trenches between adjacent structure elements, results in a simultaneous flattening and broadening of the residence time distribution.

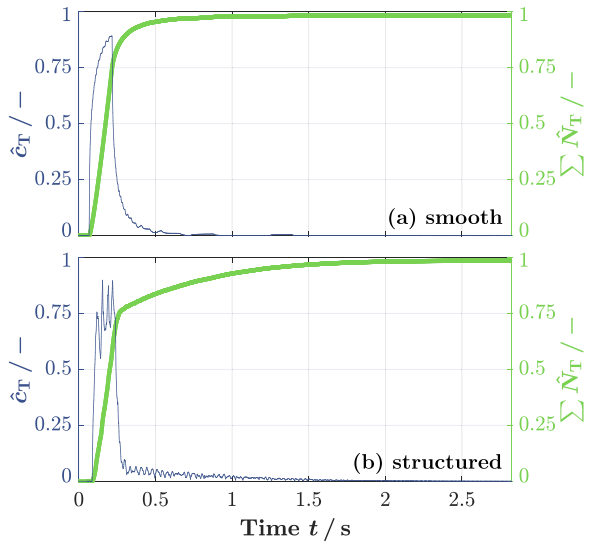

Fig. 16. Temporal evolution of the mean tracer concentration $\hat{c}_T = c_T/c_{T,in}$ (left) and cumulative amount of species $\Sigma\hat{N}_T = \Sigma N_T/N_{T,in}$ (right) at the probe line 1 in Fig. 14a. The dimensionless results are given for the smooth reference plate (a) and the structured surface with $H_s = 0.45$ mm and $D_s = 4$ mm (b). $Re = 342$.

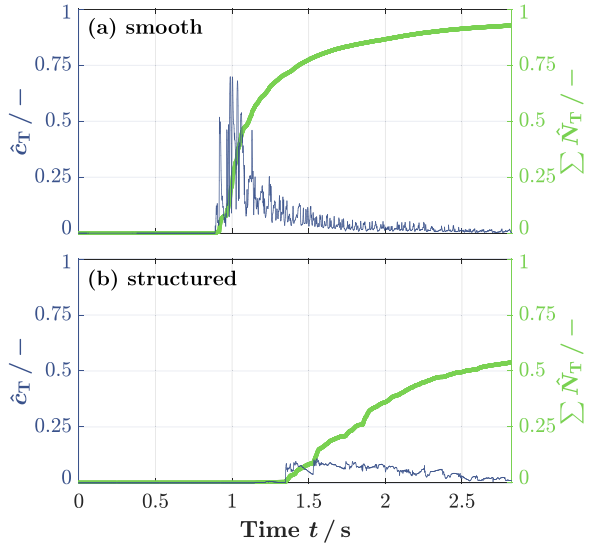

Fig. 17. Temporal evolution of the tracer concentration (left) and cumulative amount of species (right) at the probe line 2 in Fig. 14a. The dimensionless results are given for the smooth reference plate (a) and the structured surface with $H_s = 0.45$ mm and $D_s = 4$ mm (b). $Re = 342$.

Thus, compared to the smooth surface, the overall residence time is considerably increased ($\tau = 2.5$ s). On the one hand, these observations underline the efficient structure-induced mixing effects in the case of properly chosen structure dimensions. On the other hand, this points to potential limitations of integrating surface structuring in applications where short liquid residence times are important.

6. Conclusion

Wave resonance effects in falling film flows on structured surfaces have been extensively studied from a hydrodynamics perspective. Our contribution broadens this focus by examining their implications for mass transfer applications, such as CO_2 capture in falling film absorbers.

The surface structures investigated induce time-oscillatory interface motion, and local film thickness measurements show that their wave dynamics differ significantly from those of solitary waves on smooth surfaces. Most importantly, the structure-induced interface deformation is characterized by a dynamic interplay of low-frequency and high-frequency wave structures, with no clear spatial separation between adjacent wave fronts. The structure dimensions must be carefully optimized to achieve maximum wave intensity under resonance-like conditions. This enhanced interface motion is directly reflected in the mass transfer characteristics, with CO_2 absorption experiments revealing an increase in the volumetric mass transfer coefficient up to a factor of 4.1 compared to the smooth reference plate.

Complementary numerical simulations provide novel insights into the underlying mass transfer enhancement mechanisms. The structure-induced increase in gas–liquid interfacial area plays a minor role in the overall mass transfer enhancement, with structure-related changes in the internal flow conditions being the dominant contributor. Most importantly, convective mixing zones in steep wave humps upstream of flow reversal zones transport clusters of high CO_2 concentration from near the interface toward the less saturated bulk liquid. Unlike solitary waves on smooth surfaces, the elevated wave humps merge back into less distorted interface regions after passing a few structure elements, thereby promoting homogenization of the CO_2 concentration across the entire liquid film. At the same time, however, the liquid residence time distribution is significantly broadened, indicating that the suitability of specific types of surface structuring is dependent on the intended application. Limitations may arise in cases where short or well-defined residence times are required. In this context, it would be interesting to explore whether altered structure geometries, e.g. ridges with triangular or circular cross-sections, could narrow the liquid residence time distribution while preserving the resonance effect.

Since the simulations were limited to a two-dimensional domain, potential structure-induced mixing effects in the spanwise direction could not be captured numerically. In falling film flows on smooth surfaces, the evolution of three-dimensional wave structures from two-dimensional wave fronts was shown to partially disrupt the large recirculation vortices forming in the solitary wave humps [53]. At the same time, pronounced spanwise liquid motion was reported to occur in regions where adjacent wave structures interact [62,63], playing a crucial role in enhancing liquid-side transport processes [51]. Building on these observations for smooth surfaces, future studies should investigate the yet unexplored role of spanwise mixing for structured surfaces, both in intensifying heat and mass transfer in falling film devices in general, and in enhancing CO_2 absorption in falling film absorbers in particular.

CRediT authorship contribution statement

Andrea Düll: Writing – review & editing, Writing – original draft, Visualization, Validation, Software, Methodology, Investigation, Formal analysis, Data curation, Conceptualization. **Andreas Happ:** Investigation. **Jakob Buchmüller:** Investigation. **Cihan Ateş:** Supervision, Funding acquisition, Conceptualization. **Marion Börnhorst:** Writing – review & editing, Supervision, Funding acquisition, Conceptualization. **Thomas Häber:** Writing – review & editing, Validation, Supervision, Project administration, Funding acquisition. **Olaf Deutschmann:** Writing – review & editing, Supervision, Resources.

Declaration of competing interest

The authors declare that they have no known competing financial interests or personal relationships that could have appeared to influence the work reported in this paper.

Acknowledgments

The authors thank Prof. Hans-Jörg Bauer and Dr. Rainer Koch for fruitful scientific discussions and for providing experimental equipment. Financial support by the Friedrich and Elisabeth Boysen Foundation (Project-ID Boy-165) and the Helmholtz program 'Materials and Technologies for the Energy Transition, Germany' (MTET, 38.03.04) is gratefully acknowledged. The authors acknowledge support by the state of Baden-Württemberg through bwHPC.

Appendix A. CO_2 absorption and the carbonate system

At the gas–liquid interface, gaseous CO_2 (g) is absorbed into the liquid phase (Eq. (A.1)) [64]. The corresponding thermodynamic equilibrium is described by Henry's law, which relates the liquid phase CO_2 concentration c_{CO_2} to its partial pressure in the gas phase p_{CO_2} (Eq. (A.2)) [65].

$$CO_2\,(g) \rightleftharpoons CO_2 \tag{A.1}$$

$$H_{CO_2} = \frac{c_{CO_2}}{p_{CO_2}} \quad \text{with} \quad p_{CO_2} = y_{CO_2} p \tag{A.2}$$

In a subsequent step, hydrogencarbonate HCO_3^- can be formed through a hydration reaction (see Eq. (A.3)) [64]. Eq. (A.4) gives the corresponding reaction equilibrium constant K_1 [64].

$$\text{R1:} \quad CO_2 + H_2O \rightleftharpoons HCO_3^- + H^+ \tag{A.3}$$

$$K_1 = \frac{c_{HCO_3^-}\, c_{H^+}}{c_{CO_2}} \tag{A.4}$$

Afterward, carbonate CO_3^{2-} can be formed from hydrogencarbonate HCO_3^- through a protolysis mechanism (Eqs. (A.5) and (A.6)) [64].

$$\text{R2:} \quad HCO_3^- \rightleftharpoons CO_3^{2-} + H^+ \tag{A.5}$$

$$K_2 = \frac{c_{CO_3^{2-}}\, c_{H^+}}{c_{HCO_3^-}} \tag{A.6}$$

The acidic reaction pathway described above is coupled to a complementary alkaline reaction pathway by the auto-dissociation of water (Eqs. (A.7) and (A.8)) [66].

$$H_2O \rightleftharpoons H^+ + OH^- \tag{A.7}$$

$$K_w = c_{H^+} c_{OH^-} \tag{A.8}$$

The temperature-dependent equilibrium constants are calculated according to Appendix C.3.

Appendix B. Calculation of species concentrations as a function of *pH*

Assuming chemical equilibrium and electroneutrality, the individual species concentrations c_i are calculated according to Eqs. (B.1)–(B.8) in units of mol/l. For physical CO_2 absorption, the amount of chemically absorbed carbon species is negligibly small, i.e. $c_{\Sigma C} \approx c_{CO_2}$.

- Hydrogen ion H^+:

$$c_{H^+} = 10^{-pH} \tag{B.1}$$

- Hydroxide OH^-:

$$c_{OH^-} = \frac{K_w}{c_{H^+}} \tag{B.2}$$

- Overall carbon species C:

$$c_{\Sigma C} = c_{CO_2} + c_{HCO_3^-} + c_{CO_3^{2-}} \tag{B.3}$$

$$c_{\Sigma C} = \left(c_{Na^+} - c_{Cl^-} + c_{H^+} - \frac{K_w}{c_{H^+}} \right) X_1 \tag{B.4}$$

$$X_1 = \left(\frac{\frac{c_{H^+}^2}{K_1 K_2} + \frac{c_{H^+}}{K_2} + 1}{2 + \frac{c_{H^+}}{K_2}} \right) \tag{B.5}$$

- Carbonate HCO_3^-:

$$c_{CO_3^{2-}} = \frac{c_{\Sigma C}}{\frac{c_{H^+}^2}{K_1 K_2} + \frac{c_{H^+}}{K_2} + 1} \tag{B.6}$$

- Hydrogencarbonate HCO_3^-:

$$c_{HCO_3^-} = \left(\frac{c_{H^+}}{K_2} \right) c_{CO_3^{2-}} \tag{B.7}$$

- Aqueous carbon dioxide CO_2:

$$c_{CO_2} = \frac{c_{HCO_3^-} c_{H^+}}{K_1} \tag{B.8}$$

Appendix C. Calculation of equilibrium constants and transport properties

C.1. Solubility

The Henry constant of CO_2 in H_2O in calculated from Eq. (C.1), which was fitted by Sander [65] to data from Dean and Lange [67].

$$H_{CO_2} = \exp\left(-138.54 + \frac{7859.16}{T/K} + 18.28 \ln(T/K) \right) \frac{\text{mol}}{\text{m}^3\,\text{Pa}} \tag{C.1}$$

C.2. Diffusivity

The diffusion coefficient of CO_2 dissolved in H_2O $D_{CO_2,L}$ is calculated according to Eq. (C.2) [68].

$$D_{CO_2,L} = 2.35 \times 10^{-6} \exp\left(\frac{-2119}{T/K} \right) \frac{\text{m}^2}{\text{s}} \tag{C.2}$$

The self-diffusivity of gaseous CO_2 $D_{CO_2,G}$ is estimated on the basis of Eq. (C.3), which was fitted to data from [69].

$$D_{CO_2,G} = (79.62\,T/K - 12446) \times 10^{-9} \frac{\text{m}^2}{\text{s}} \tag{C.3}$$

C.3. Reaction equilibria

The reaction equilibrium constants are calculated according to Eq. (C.4) [70], Eq. (C.5) [71] and Eq. (C.6) [72]. The density of the solution is $\rho \approx 1\,\text{kg/l}$.

$$K_1 = 10\hat{}\left(-\frac{3404.71}{T/K} - 0.032786\,T/K + 14.8435 \right) \frac{\text{mol}}{\text{kg}} \rho \tag{C.4}$$

$$K_3 = 10\hat{}\left(-\frac{2902.39}{T/K} - 0.02379\,T/K + 6.4980 \right) \frac{\text{mol}}{\text{kg}} \rho \tag{C.5}$$

$$K_w = \exp\left(148.9802 - \frac{13847.26}{T/K} - 23.6521 \ln(T/K) \right) \frac{\text{mol}^2}{\text{kg}^2} \rho^2 \tag{C.6}$$

Table D.2
Grid convergence parameters obtained from mass transfer simulations on the smooth reference plate.

Property	c_{CO_2}	kA	A	s_h
r_{32}			1.32	
r_{21}			1.34	
e_{32}	3.38%	6.05%	0.08%	10.19%
e_{21}	1.62%	3.00%	0.07%	3.92%
p_{GCI}	2.64	2.58	0.57	3.34
$GCI_{f,32}$	3.84%	7.12%	0.61%	8.19%
$GCI_{f,21}$	1.75%	3.35%	0.51%	2.98%
AR_{GCI}	0.97	0.98	1.00	0.94

Appendix D. Grid convergence

Table D.2 provides grid convergence parameters for key output variables, namely the CO_2 concentration c_{CO_2}, the volumetric mass transfer coefficient kA, the gas–liquid interfacial area A, and the film thickness standard deviation s_h. The latter is determined at probe line 2 in Fig. 14. The calculation procedure follows the methodology proposed in the literature [73,74]. The results are obtained from mass transfer simulations on the smooth reference plate. In the table, r_{ij} is the refinement ratio from a coarser to a finer grid, e_{ij} is the error of a variable of interest between two grids, p_{GCI} is the iteratively determined apparent order of approximation, $GCI_{f,ij}$ is the grid convergence index for the respective fine-grid solution, and AR_{GCI} is an indicator for whether the calculations are within the asymptotic range of convergence ($AR_{GCI} \rightarrow 1$). Indices 1, 2, and 3 correspond to the fine, medium, and coarse grids, respectively. The fine grid was selected for the remainder of the study to ensure that the GCI_f values remained below 5% for all monitored parameters.

Appendix E. Supplementary data

Supplementary material related to this article can be found online at https://doi.org/10.1016/j.cej.2025.168228.

Data availability

Data will be made available on request.

References

[1] G. Cravotto, Reshaping chemical manufacturing towards green process intensification: Recent findings and perspectives, Processes 13 (2) (2025) http://dx.doi.org/10.3390/pr13020459.

[2] G.G. Jang, J.A. Thompson, X. Sun, C. Tsouris, Process intensification of CO2 capture by low-aqueous solvent, Chem. Eng. J. 426 (2021) 131240, http://dx.doi.org/10.1016/j.cej.2021.131240.

[3] R. Notz, H.P. Mangalapally, H. Hasse, Post combustion CO2 capture by reactive absorption: Pilot plant description and results of systematic studies with MEA, Int. J. Greenh. Gas Control. 6 (2012) 84–112, http://dx.doi.org/10.1016/j.ijggc.2011.11.004.

[4] E. Pahija, S. Golshan, B. Blais, D.C. Boffito, Perspectives on the process intensification of CO2 capture and utilization, Chem. Eng. Process. - Process. Intensif. 176 (2022) 108958, http://dx.doi.org/10.1016/j.cep.2022.108958.

[5] A.A. Kiss, R. Smith, Rethinking energy use in distillation processes for a more sustainable chemical industry, Energy 203 (2020) 117788, http://dx.doi.org/10.1016/j.energy.2020.117788.

[6] F.J. Keil, Process intensification, Rev. Chem. Eng. 34 (2) (2018) 135–200, http://dx.doi.org/10.1515/revce-2017-0085.

[7] M. Kohrt, Experimentelle Untersuchung Von Stofftransport Und Fluiddynamik Bei Rieselfilmstromungen Auf Mikrostrukturierten Oberflächen (Ph.D. thesis), TU Berlin, 2012, Retrieved from https://doi.org/10.14279/depositonce-3208.

[8] M. Al-Rawashdeh, A. Cantu-Perez, D. Ziegenbalg, P. Löb, A. Gavriilidis, V. Hessel, F. Schönfeld, Microstructure-based intensification of a falling film microreactor through optimal film setting with realistic profiles and in-channel induced mixing, Chem. Eng. J. 179 (2012) 318–329, http://dx.doi.org/10.1016/j.cej.2011.11.014.

[9] D. Sebastia-Saez, S. Gu, P. Ranganathan, K. Papadikis, 3D modeling of hydrodynamics and physical mass transfer characteristics of liquid film flows in structured packing elements, Int. J. Greenh. Gas Control. 19 (2013) 492–502, http://dx.doi.org/10.1016/j.ijggc.2013.10.013.

[10] H. Rößler, W. Wiesenhofer, C. Glasmacher-Remberg, C. Breucker, Thin-film reactors, in: Ullmann's Encyclopedia of Industrial Chemistry, Wiley-VCH, Weinheim, 2013.

[11] Z. Dai, Y. Zhang, S. Wang, K. Nawaz, A. Jacobi, Falling-film heat exchangers used in desalination systems: A review, Int. J. Heat Mass Transfer 185 (2022) 122407, http://dx.doi.org/10.1016/j.ijheatmasstransfer.2021.122407.

[12] M. Le Page Mostefa, H. Muhr, A. Biget, E. Palasari, M. Fauconet, Intensification of falling film melt crystallization process through micro and milli-structured surfaces, Chem. Eng. Process.: Process. Intensif. 90 (2015) 16–23, http://dx.doi.org/10.1016/j.cep.2015.02.006.

[13] M. Mortazavi, R. Nasr Isfahani, S. Bigham, S. Moghaddam, Absorption characteristics of falling film LiBr (lithium bromide) solution over a finned structure, Energy 87 (2015) 270–278, http://dx.doi.org/10.1016/j.energy.2015.04.074.

[14] A. Charogiannis, J.S. An, C.N. Markides, A simultaneous planar laser-induced fluorescence, particle image velocimetry and particle tracking velocimetry technique for the investigation of thin liquid-film flows, Exp. Therm. Fluid Sci. 68 (2015) 516–536, http://dx.doi.org/10.1016/j.expthermflusci.2015.06.008.

[15] A.A. Alhusseini, K. Tuzla, J.C. Chen, Falling film evaporation of single component liquids, Int. J. Heat Mass Transfer 41 (12) (1998) 1623–1632, http://dx.doi.org/10.1016/S0017-9310(97)00308-6.

[16] A. Åkesjö, M. Gourdon, L. Vamling, F. Innings, S. Sasic, Modified surfaces to enhance vertical falling film heat transfer – An experimental and numerical study, Int. J. Heat Mass Transfer 131 (2019) 237–251, http://dx.doi.org/10.1016/j.ijheatmasstransfer.2018.11.061.

[17] S. Chen, T. Zhang, L. Lv, Y. Chen, S. Tang, Simulation of the hydrodynamics and mass transfer in a falling film wavy microchannel, Chin. J. Chem. Eng. 34 (2021) 97–105, http://dx.doi.org/10.1016/j.cjche.2020.09.014.

[18] J. Davies, K. Warner, The effect of large-scale roughness in promoting gas absorption, Chem. Eng. Sci. 24 (2) (1969) 231–240, http://dx.doi.org/10.1016/0009-2509(69)80032-1.

[19] H. Lu, L. Lu, X. Gao, Mass transfer enhancement of falling film liquid desiccant dehumidification by micro-baffle plates, Int. J. Heat Mass Transfer 169 (2021) 120945, http://dx.doi.org/10.1016/j.ijheatmasstransfer.2021.120945.

[20] S. Negny, M. Meyer, M. Prévost, Modelling of the coupling hydrodynamic transfer for a gas–liquid countercurrent flow on a wavy surface, Chem. Eng. Sci. 58 (12) (2003) 2705–2714, http://dx.doi.org/10.1016/S0009-2509(03)00123-4.

[21] L. Zhao, R. Cerro, Experimental characterization of viscous film flows over complex surfaces, Int. J. Multiph. Flow 18 (4) (1992) 495–516, http://dx.doi.org/10.1016/0301-9322(92)90048-L.

[22] Y. Lu, F. Stehmann, S. Yuan, S. Scholl, Falling film on a vertical flat plate – Influence of liquid distribution and fluid properties on wetting behavior, Appl. Therm. Eng. 123 (2017) 1386–1395, http://dx.doi.org/10.1016/j.applthermaleng.2017.05.110.

[23] H. Ishikawa, S. Ookawara, S. Yoshikawa, H. Matsumoto, Numerical study on mass transfer in a falling film on structured plates with micro-baffles, Chem. Eng. Process. - Process. Intensif. 175 (2022) 108903, http://dx.doi.org/10.1016/j.cep.2022.108903.

[24] S. Paschke, Experimentelle Analyse Ein- Und Zweiphasiger Filmströmungen Auf Glatten Und Strukturierten Oberflächen (Ph.D. thesis), TU Berlin, 2011, Retrieved from https://doi.org/10.14279/depositonce-3069.

[25] A. Düll, A. Cros-Le Lagadec, J. Buchmüller, T. Häber, C. Ates, M. Börnhorst, Intensifying Interfacial Oscillations in Falling Film Flows Over Rectangular Corrugations, Phys. Fluids 36 (9) (2024) 092107, http://dx.doi.org/10.1063/5.0222760.

[26] A. Düll, J. Lehmann, M. Börnhorst, C. Ateş, T. Häber, O. Deutschmann, Spatio-temporal characterization of the three-dimensional wave dynamics in falling film flows over rectangular corrugations, Exp. Fluids 66 (71) (2025) http://dx.doi.org/10.1007/s00348-025-03978-2.

[27] Precitec, Overview chromatic confocal point sensors, 2021, https://www.precitec.com. (Accessed 12 December 2022).

[28] J.F. Chambers, J.M. Stokes, R.H. Stokes, Conductances of concentrated aqueous sodium and potassium chloride solutions at 25°, J. Phys. Chem. 60 (7) (1956) 985–986, http://dx.doi.org/10.1021/j150541a040.

[29] S. Kalliadasis, C. Ruyer-Quil, B. Scheid, M.G. Velarde, Falling Liquid Films, Springer London, 2012.

[30] M. Kraume, Transportvorgänge in Der Verfahrenstechnik, Springer Vieweg Berlin, Heidelberg, 2020.

[31] GeoChemFoam-5.0, 2023, https://github.com/GeoChemFoam/GeoChemFoam-5.0, Downloaded 11 August 2024.

[32] J. Maes, H.P. Menke, GeoChemFoam: Direct modelling of multiphase reactive transport in real pore geometries with equilibrium reactions, Transp. Porous Media 139 (2) (2021) 271–299, http://dx.doi.org/10.1007/s11242-021-01661-8.

[33] J. Maes, H.P. Menke, A bespoke OpenFOAM toolbox for multiphysics flow simulations in pore structures, in: Proceedings of the 17th International Conference on Flow Dynamics, 2020.

[34] J. Maes, H.P. Menke, GeoChemFoam: Direct modelling of flow and heat transfer in micro-CT images of porous media, Heat Mass Transf. 58 (11) (2022) 1937–1947, http://dx.doi.org/10.1007/s00231-022-03221-2.
[35] C. Hirt, B. Nichols, Volume of fluid (VOF) method for the dynamics of free boundaries, J. Comput. Phys. 39 (1) (1981) 201–225, http://dx.doi.org/10.1016/0021-9991(81)90145-5.
[36] J. Maes, C. Soulaine, A new compressive scheme to simulate species transfer across fluid interfaces using the Volume-Of-Fluid method, Chem. Eng. Sci. 190 (2018) 405–418, http://dx.doi.org/10.1016/j.ces.2018.06.026.
[37] J. Brackbill, D. Kothe, C. Zemach, A continuum method for modeling surface tension, J. Comput. Phys. 100 (2) (1992) 335–354, http://dx.doi.org/10.1016/0021-9991(92)90240-Y.
[38] J. Maes, GeoChemFoam user guide, 2022, https://github.com/GeoChemFoam/GeoChemFoam-4.6/blob/main/doc/GeoChemFoam-User-Guide.pdf, (Accessed 11 August 2024).
[39] M.M. Francois, S.J. Cummins, E.D. Dendy, D.B. Kothe, J.M. Sicilian, M.W. Williams, A balanced-force algorithm for continuous and sharp interfacial surface tension models within a volume tracking framework, J. Comput. Phys. 213 (1) (2006) 141–173, http://dx.doi.org/10.1016/j.jcp.2005.08.004.
[40] A.Q. Raeini, M.J. Blunt, B. Bijeljic, Modelling two-phase flow in porous media at the pore scale using the volume-of-fluid method, J. Comput. Phys. 231 (17) (2012) 5653–5668, http://dx.doi.org/10.1016/j.jcp.2012.04.011.
[41] O. Ltd, Hydrostatic pressure effects, 2023, https://doc.openfoam.com/2212/tools/processing/solvers/algorithm-p-rgh/, (Accessed 21 February 2025).
[42] J. Maes, C. Soulaine, A unified single-field volume-of-fluid-based formulation for multi-component interfacial transfer with local volume changes, J. Comput. Phys. 402 (2020) 109024, http://dx.doi.org/10.1016/j.jcp.2019.109024.
[43] N. Samkhaniani, A. Stroh, Simulation of single vapor bubble condensation with sharp interface mass transfer model, Thermo 2 (3) (2022) 149–159, http://dx.doi.org/10.3390/thermo2030012.
[44] T. Nakano, M.A. Bucci, J.-M. Gratien, T. Faney, Machine learning model for gas–liquid interface reconstruction in CFD numerical simulations, Fluids 10 (1) (2025) http://dx.doi.org/10.3390/fluids10010020.
[45] J. Wojtkowiak, C.O. Popiel, Inherently linear annular-duct-type laminar flowmeter, J. Fluids Eng. 128 (1) (2005) 196–198, http://dx.doi.org/10.1115/1.2137347.
[46] A.E. Al-Rawajfeh, Modelling and Simulation of CO_2 Release in Multiple-Effect Distillers for Seawater Desalination (Ph.D. thesis), Martin Luther University Halle-Wittenberg, 2004, Retrieved from http://dx.doi.org/10.25673/3764.
[47] N. Pallas, B. Pethica, The surface tension of water, Colloids Surf. 6 (3) (1983) 221–227, http://dx.doi.org/10.1016/0166-6622(83)80014-6.
[48] W. Wagner, H.-J. Kretzschmar, Wasser, in: V.D.I. e.V. (Ed.), VDI-WÄrmeatlas, Springer Vieweg, Berlin, Heidelberg, 2013.
[49] R. Span, Kohlendioxid, in: V.D.I. e.V. (Ed.), VDI-WÄrmeatlas, Springer Vieweg, Berlin, Heidelberg, 2013.
[50] F. Al-Sibai, Experimentelle Untersuchung Der Strömungscharakteristik Und Des Wärmeübergangs Bei Welligen Rieselfilmen (Ph.D. thesis), RWTH Aachen University, 2004, Retrieved from https://nbn-resolving.org/urn:nbn:de:hbz:82-20050535.
[51] A. Schagen, Methode Der Laser-Induzierten Lumineszenz Zur Experimentellen Analyse Des Stofftransportes in Laminar-Welligen Flüssigkeitsfilmen (Ph.D. thesis), RWTH Aachen University, 2014, Retrieved from https://nbn-resolving.org/urn:nbn:de:hbz:82-rwth-2015-021913.
[52] N. Brauner, D.M. Maron, Characteristics of inclined thin films, waviness and the associated mass transfer, Int. J. Heat Mass Transfer 25 (1) (1982) 99–110, http://dx.doi.org/10.1016/0017-9310(82)90238-1.
[53] C.D. Park, T. Nosoko, Three-dimensional wave dynamics on a falling film and associated mass transfer, AIChE J. 49 (11) (2003) 2715–2727, http://dx.doi.org/10.1002/aic.690491105.
[54] B. Al-Shamaa, T. Kahraman, A. Wierschem, Steady three-dimensional patterns in gravity-driven film flow down an inclined sinusoidal bottom contour, Phys. Fluids 35 (3) (2023) 033307, http://dx.doi.org/10.1063/5.0140841.
[55] M. Vlachogiannis, V. Bontozoglou, Experiments on laminar film flow along a periodic wall, J. Fluid Mech. 457 (2002) 133–156, http://dx.doi.org/10.1017/S0022112001007637.
[56] V. Bontozoglou, K. Serifi, Falling film flow along steep two-dimensional topography: The effect of inertia, Int. J. Multiph. Flow 34 (8) (2008) 734–747, http://dx.doi.org/10.1016/j.ijmultiphaseflow.2008.01.006.
[57] S. Ishigai, S. Nakanisi, T. Koizumi, Z. Oyabu, Hydrodynamics and heat transfer of vertical falling liquid films : Part 1, classification of flow regimes, Bull. JSME 15 (83) (1972) 594–602, http://dx.doi.org/10.1299/jsme1958.15.594.
[58] S.-M. Yih, K.-Y. Chen, Gas absorption into wavy and turbulent falling liquid films in a wetted-wall column, Chem. Eng. Commun. 17 (1–6) (1982) 123–136, http://dx.doi.org/10.1080/00986448208911620.
[59] G.F. Dietze, Effect of wall corrugations on scalar transfer to a wavy falling liquid film, J. Fluid Mech. 859 (2019) 1098–1128, http://dx.doi.org/10.1017/jfm.2018.851.
[60] F. Denner, A. Charogiannis, M. Pradas, C.N. Markides, B.G.M. van Wachem, S. Kalliadasis, Solitary waves on falling liquid films in the inertia-dominated regime, J. Fluid Mech. 837 (2018) 491–519, http://dx.doi.org/10.1017/jfm.2017.867.
[61] N.A. Malamataris, V. Balakotaiah, Flow structure underneath the large amplitude waves of a vertically falling film, AIChE J. 54 (7) (2008) 1725–1740, http://dx.doi.org/10.1002/aic.11506.
[62] R.K. Georg F. Dietze, Flow separation in falling liquid films, Front. Heat Mass Transf. 2 (3) (2011) 1–14, http://dx.doi.org/10.5098/hmt.v2.3.3001.
[63] G.F. Dietze, W. Rohlfs, K. Nährich, R. Kneer, B. Scheid, Three-dimensional flow structures in laminar falling liquid films, J. Fluid Mech. 743 (2014) 75–123, http://dx.doi.org/10.1017/jfm.2013.679.
[64] R.E. Zeebe, D. Wolf-Gladrow, CO2 in Seawater: Equilibrium, Kinetics, Isotopes, Elsevier Oceanography Series, vol. 65, Elsevier, 2001.
[65] R. Sander, Compilation of Henry's law constants (version 5.0.0) for water as solvent, Atmospheric Chem. Phys. 23 (19) (2023) 10901–12440, http://dx.doi.org/10.5194/acp-23-10901-2023.
[66] M. Krauß, R. Rzehak, Reactive absorption of CO2 in NaOH: Detailed study of enhancement factor models, Chem. Eng. Sci. 166 (2017) 193–209, http://dx.doi.org/10.1016/j.ces.2017.03.029.
[67] J.A. Dean, N.A. Lange, Lange's Handbook of Chemistry, 15th, McGraw-Hill, Inc., 1999.
[68] G.F. Versteeg, W.P.M. Van Swaaij, Solubility and diffusivity of acid gases (carbon dioxide, nitrous oxide) in aqueous alkanolamine solutions, J. Chem. Eng. Data 33 (1) (1988) 29–34, http://dx.doi.org/10.1021/je00051a011.
[69] O. Suárez-Iglesias, I. Medina, M.d.l.Á. Sanz, C. Pizarro, J.L. Bueno, Self-diffusion in molecular fluids and noble gases: Available data, J. Chem. Eng. Data 60 (10) (2015) 2757–2817, http://dx.doi.org/10.1021/acs.jced.5b00323.
[70] H.S. Harned, R.J. Davis, The ionization constant of carbonic acid in water and the solubility of carbon dioxide in water and aqueous salt solutions from 0 to 50°, J. Am. Chem. Soc. 65 (10) (1943) 2030–2037, http://dx.doi.org/10.1021/ja01250a059.
[71] H.S. Harned, S.R.J. Scholes, The ionization constant of HCO3- from 0 to 50°, J. Am. Chem. Soc. 63 (6) (1941) 1706–1709, http://dx.doi.org/10.1021/ja01851a058.
[72] F.J. Millero, Thermodynamics of the carbon dioxide system in the oceans, Geochim. Cosmochim. Acta 59 (4) (1995) 661–677, http://dx.doi.org/10.1016/0016-7037(94)00354-O.
[73] P.J. Roache, Perspective: A method for uniform reporting of grid refinement studies, J. Fluids Eng. 116 (3) (1994) 405–413, http://dx.doi.org/10.1115/1.2910291.
[74] I. Celik, U. Ghia, P. Roache, C. Freitas, H. Coloman, P. Raad, Procedure for estimation and reporting of uncertainty due to discretization in CFD applications, J. Fluids Eng. 130 (7) (2008) 078001, http://dx.doi.org/10.1115/1.2960953.